Final_thesis_kjeld_broekema.pdf

by Kjeld Broekema

Submission date: 11-May-2021 10:23PM (UTC+0200)
Submission ID: 1583858225
File name: Final_thesis_kjeld_broekema.pdf (5.79M)
Word count: 23885
Character count: 114440

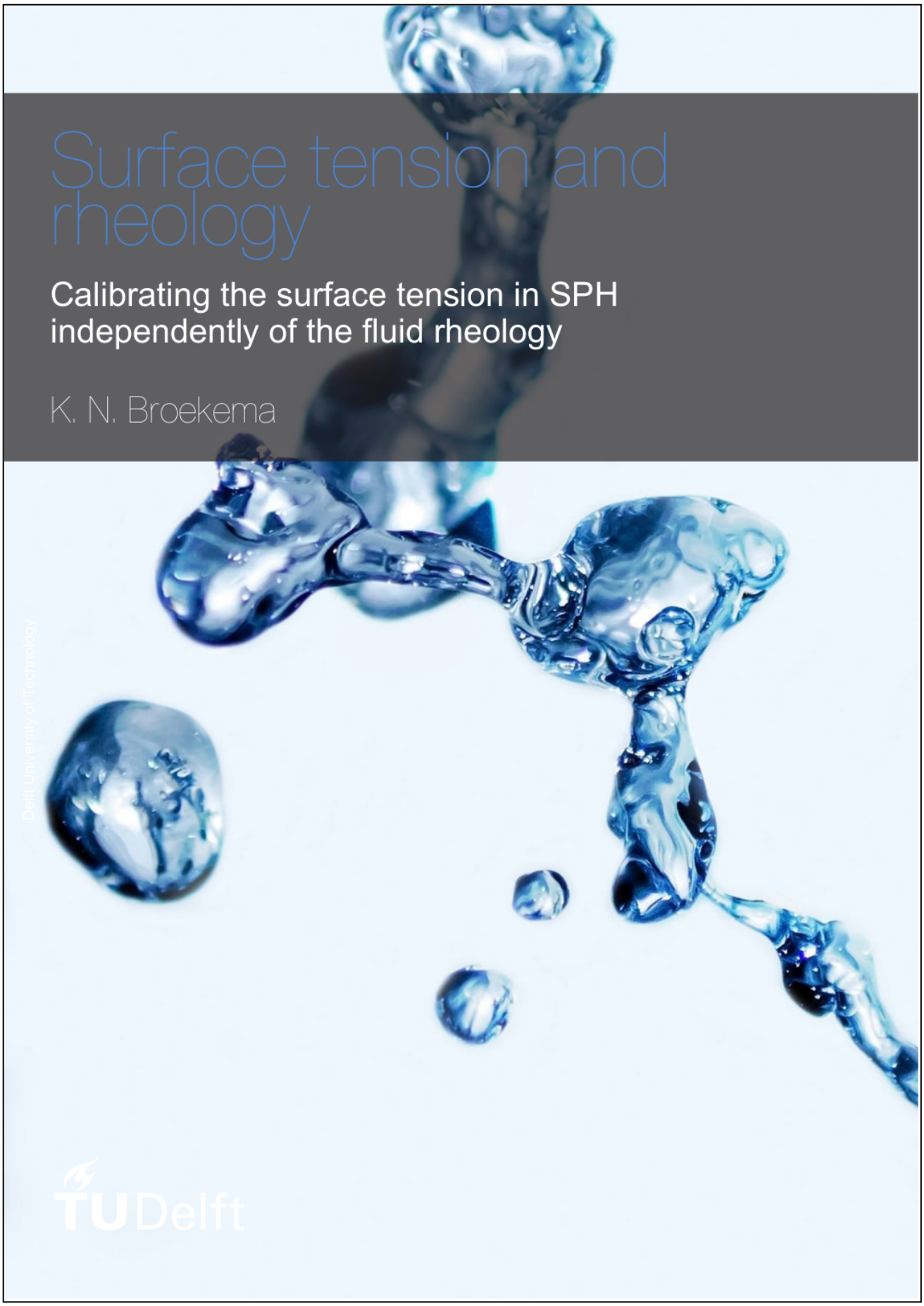

Surface tension and rheology

Calibrating the surface tension in SPH independently of the fluid rheology

K. N. Broekema

Delft University of Technology

TU Delft

Surface tension and rheology

Calibrating the surface tension in SPH independently of the fluid rheology

by

K. N. Broekema

to obtain the degree of Master of Science
at the Delft University of Technology,
to be defended publicly on Tuesday May 25, 2021 at 10:00 AM.

Student number:	4378644	
Project duration:	August 1, 2020 – May 25, 2021	
Thesis committee:	Prof. dr. ir. K. Vuik	TU Delft, supervisor
	Prof. dr. ir. J. T. Padding	TU Delft, supervisor
	Prof. dr. ir. A. W. Heemink	TU Delft
	Ir. S. Sneijders	TU Delft, supervisor

Colliding water droplets. Image from `https://www.pikist.com/free-photo-sayym`.

TU Delft

Preface

This thesis has been written to fulfil the final graduation requirement to obtain a master degree in Applied Mathematics at the Delft University of Technology. I would like to take this opportunity to thank my supervisors (Prof. dr. ir. K. Vuik, Prof. dr. ir. J. T. Padding and Ir. S. Sneijders) for their guidance and support during this process. Especially their flexibility, which was needed due to the COVID-19 pandemic. Additionally, I am grateful for Ir. T. Mager for his assistance with the SiPER code. Furthermore, I would like to thank my roommates for breaking the Corona rut, which gave me new energy to finish this thesis. Last but certainly not least, my deepest gratitude goes out to my family and girlfriend for their unending support and interest, where I would like to specifically thank my brother Yorick for his guidance during my bachelor and master.

K. N. Broekema
Delft, May 2021

Abstract

Spray drying operations can be used to turn products, like for example milk or yeast extract, into powders, extending their shelf life. The properties of those powders (e.g. density or particle size) after spray drying operations depend severely on the dynamics of droplet collisions inside the spray. Currently, costly and wasteful production-trials are used in the spray drying industry. The use of computer models can potentially reduce those costs significantly. However, present-day models lack a complete physical foundation to supersede these trial-and-error tests. This study aims to further develop implementation of the relevant physical processes in these models by incorporating the combined effect of rheology and surface tension.

In this thesis, we quantify the effect of Particle Interaction Forces (PIF) on the surface tension and investigate the possibility to further calibrate the PIF induced surface tension to match the desired surface tension. Important here is that we do not change the PIF induced rheology. We make use of the numerical method Smoothed Particle Hydrodynamics (SPH) and use the Continuum Surface Force (CSF) method to further tune the surface tension. We demonstrate the tuning properties of CSF in a static and a dynamic setting. Because the constitutive equation of the PIF induced rheology is unknown, we are limited in the possible dynamic tests in which we assess the relation between the rheology and surface tension. The dynamic tests that we could perform in this thesis are characterized by the surface tension being dominant with respect to the viscosity and elasticity of the droplet.

In the static case, we found that we can estimate the magnitude of the PIF induced surface tension and increase the surface tension with CSF to the desired value. Furthermore, for the static case, when both CSF and PIF are used, the total surface tension is simply the sum of the separate forces, i.e. CSF and PIF are decoupled forces. Additionally, preliminary results suggest that we can also lower the PIF induced surface tension to a certain extent, by adding CSF with a negative coefficient. However, the dynamic test results are not straightforwardly interpreted, probably due to not satisfying the assumption that the surface tension is the dominant contribution. Therefore, these tests are inconclusive and thus require further research.

Contents

Nomenclature

Abbreviations

Abbreviation	Definition
CFL	Courant-Friedrichs-Lewy
CSF	Continuum Surface Force
FD	Finite Difference
FEM	Finite Elements Methods
ISPH	Incompressible Smoothed Particle Hydrodynamics
PIF	Particle Interaction Forces
PISMF	Particle Interaction Surface Minimization Force
SPH	Smoothed Particle Hydrodynamics
WCSPH	Weakly Compressible Smoothed Particle Hydrodynamics

Symbols

Symbol	Definition	Unit
a	Acceleration	[m/s^2]
c	Color function	[-]
c_0	Artificial speed of sound	[m/s]
dt	Time step	[s]
$\mathbf{F}^{int}$	Total particle interaction force vector	[N]
$\mathbf{F}^{\mu}$	Viscous force vector	[N]
$\mathbf{F}^{p}$	Pressure force vector	[N]
$\mathbf{F}_{surf}$	Surface tension body force	[N/m^3]
G	Elastic modulus	[Pa]
G'	Storage modulus	[Pa]
G''	Loss modulus	[Pa]
$\mathbf{L}$	Correction matrix	[-]
L_0	Initial particle distance	[m]
L_x	Length of the box in the x-direction	[m]
L_y	Length of the box in the y-direction	[m]
h	Smoothing length	[m]
m	Mass	[kg]
n	Numerical density	[m^{-3}]
$\mathbf{n}$	Normal vector	[m]
$\hat{\mathbf{n}}$	Unit normal vector	[-]
$\tilde{\mathbf{n}}$	Smoothed normal vector	[m]
N	Total number of particles	[-]
$\mathcal{N}$	Total number of particles within the kernel	[-]
$N_{particles}$	Maximum possible number of particles in the x-direction	[-]
$\hat{\mathbf{n}}_{wall}$	Unit normal vector to the wall boundary	[-]
p	Pressure	[Pa]
p_d	Pressure droplet	[Pa]

Symbol	Definition	Unit
p_{PIF}	Pressure in the droplet due to the PIF. That is the virial pressure and the pressure due to the PIF induced surface tension	[Pa]
p_v	Virial pressure	[Pa]
q_{cut}	Compact radius or cut-off length	[m]
R	Radius	[m]
$\mathbf{r}$	Position vector	[m]
$\mathbf{R}_d$	The center of mass vector of the whole droplet	[m]
$\bar{r}_i$	Average particle position	[m]
$\mathbf{R}_i$	Shifting vector	[m]
$\mathbf{R}_{ur}$	The center of mass vector of the upper right quarter of the droplet	[m]
S	Shepard value	[-]
$S_{\alpha\alpha}$	Interaction strength (Tartakovsky)	[N]
S_{ij}	Interaction strength (rheology)	[m/s^2]
t	Time	[s]
$\mathbf{T}_{int}$	Interaction stress vector	[Pa]
T_n	Normal stress component	[Pa]
T_τ	Tangent stress component	[Pa]
$\mathbf{u}$	Velocity vector	[m/s]
u_{max}	Maximum velocity	[m/s]
$\mathbf{u}^*$	Intermediate velocity vector	[m/s]
V	Volume	[m^3]
α	Shifting magnitude	[-]
α_{CFL}	Time step coefficient	[-]
α_d	Scaling factor	[-]
α_{diff}	Time step coefficient	[-]
γ	Strain	[-]
$\dot{\gamma}$	Strain rate	[s^{-1}]
γ_0	Strain amplitude	[-]
δ	Phase shift	[rad]
δ_s	Surface delta function	[-]
κ	Curvature	[m^{-1}]
κ	Scaling factor	[-]
$\tilde{\kappa}$	Smoothed curvature	[m^{-1}]
μ	Dynamic viscosity	[Pa.s]
μ_d	Dynamic viscosity droplet	[Pa.s]
μ_l	Dynamic viscosity surrounding liquid	[Pa.s]
ρ	Density	[kg/m^3]
ρ_d	Droplet density	[kg/m^3]
ρ_l	Surrounding fluid density	[kg/m^3]
ρ_0	Initial density	[kg/m^3]
σ	Surface tension	[N/m^2]
σ_{CSF}	CSF induced surface tension	[N/m^2]
σ_{PIF}	PIF induced surface tension	[N/m^2]
τ_{xy}	Shear stress	[Pa]
ω	Frequency	[Hz]

The units of some symbols are depended on the dimensions of space. We derived the symbol list for 3D. In general, for 2D, the spatial dimensions are reduced by one.

List of Figures

List of Tables

1 Introduction

Spray drying is a widely used technology in industries such as the food, paint and pharmaceutical industry. The food spray drying equipment market was valued at $1.2 billion in 2016 and is expected to increase to $1.6 billion by 2021 [24]. In a spray dryer droplets are converted into powders, through hot air. The droplets will enter at the top of the spray chamber, where the droplets are exposed to a heated airflow, introduced by air inlets. The resulting powder leaves the spray chamber at the bottom, see Figure 1.1 (a). During the drying, droplets will start colliding, coalesce, and agglomerate. Furthermore, droplets in different drying stadiums are involved, which increases the complexity. This will significantly influence the end-product in terms of consistency and quality; e.g. particle-size and morphology, see Figure 1.1 (b). The morphology is of great importance since this determines the properties of the end-product, such as density and solubility, which influences the end-product usability.

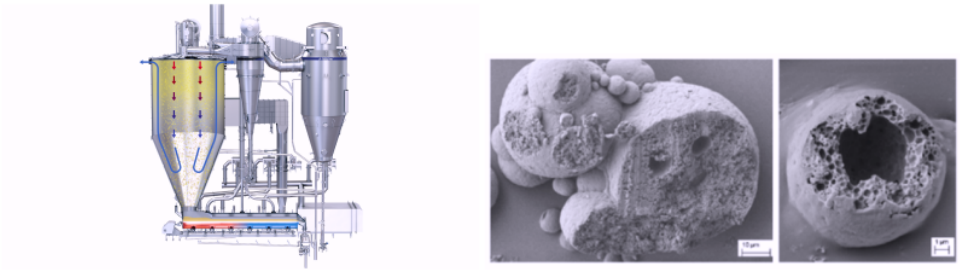

(a) (b)

Figure 1.1: (a) A schematic overview of a spray dryer. (b) Dried whole milk particles, which show the large diversity in end product particle morphology. Pictures courtesy of Tetra Pak (Sweden).

The current way to get the desired powder properties is by trial-and-error. A new product involves time-consuming and costly production-trials, where in case the end-product is not satisfactory it will be discarded. A way to avoid such costly production-trials is by introducing computer models that can simulate a spray drying process. However, current models lack the complexity, that is needed to properly simulate a drying process. Especially phenomena occurring during droplet collisions as they dry. To be able to provide more realistic simulations, a deeper understanding of the complex internal processes at the droplet scale level is needed, with the focus on simulating more realistic droplet collisions. This knowledge can then be used to improve the correlations used for collision outcomes and particle morphology development in more coarse-grained simulations.

During droplet collisions very large deformations occur which are difficult to simulate with traditional numerical methods such as Finite Elements Methods (FEM) and Finite Difference (FD) [19]. We, therefore, choose a Mesh-free method, namely Smoothed Particle Hydrodynamics (SPH). Aside from the ability to deal with large deformations other advantages of SPH are: the ability to deal with complex

(free) surfaces and multi-phases. A disadvantage, however, is the difficulty in obtaining second-order global convergence [31][1]

An obstacle in simulating realistic droplet collisions is the implementation of the correct rheological fluid properties (rheology is the science of deformation and flow). With the traditional numerical methods the fluid rheology is added through a constitutive equation[2]. However, finding the right constitutive equation and solving it, leads to a complex and troublesome task. In SPH we can avoid the usage of such complex constitutive equations, by using an alternative method, namely Particle Interaction Forces (PIF). The considered PIF generates an attraction force for distant particles and repulsion for close particles and can be thought of as breakable springs between the particles, such forces offer resistance to deformation.

In Van der Linde [40] it has been shown that PIF can be used to simulate the fluid rheology and although in [38, 3, 16] it has been shown that PIF also influences the surface tension, it is yet unknown to what extend PIF will affect the surface tension. At the droplet scale level, the surface tension is an important factor in determining if droplets will coalesce or bounce [42, 13]. Hence, to achieve realistic simulations of colliding droplets, the fluid rheology and surface tension has to be correctly modelled.

The aim of this thesis is to investigate the influence of PIF on the surface tension in order to simulate realistic fluids; i.e., how can PIF be used to calibrate the fluid rheology while adjusting surface tension independently?

To be able to answer the main question, we will first briefly explain the concept of rheology (Chapter 2), after which we will give a detailed explanation of SPH and discuss the convergence issue (Chapter 3). Next, we will investigate the possible calibration methods for the surface tension and derive an analytical estimate for the PIF induced surface tension (Chapter 4). In Chapter 5, we state the simulation details and explain the (analytical) methods that will be used to validate the numerical implementation and to measure the surface tension. Then, in Chapter 6, we will present and discuss the results of the simulations. Finally, we will finish the thesis by presenting our conclusions and recommendations for future work (Chapter 7).

[1] Order of convergence represents how fast the numerical method approaches its limit, i.e. how fast the computed solution converges to the exact solution. For a numerical method, to keep the computational time reasonable, second-order converge is needed.

[2] A constitutive equation approximates the response of a specific material to an external stimulus, i.e. relates stresses in the material to strains and strain rates.

2

Rheology

In this chapter, we will first introduce the Navier-Stokes equations for incompressible Newtonian fluids. Furthermore, the concept of non-Newtonian fluids is briefly explained. Afterwards, we will describe what viscoelastic fluids are and lastly we will explain what surface tension is and how it forms a balance with the pressure.

2.1. Navier-Stokes equations

We will omit the derivation of the momentum and continuum equations and just state them. However, if desired the derivation can be found in Morrison [28]. The equations are given by

$$\rho \frac{D\mathbf{u}}{Dt} = -\nabla p - \nabla \cdot \underline{\underline{\tau}} + \mathbf{F}_{body}, \tag{2.1}$$

$$\frac{Dp}{Dt} = -\rho \nabla \cdot \mathbf{u}, \tag{2.2}$$

where $\frac{D}{Dt}$ is the material derivative, ρ is the density, p is the pressure, $\mathbf{F}_{body}$ is the collection of all contributing body forces per unit volume (e.g. gravity, surface tension and boundary forces), $\mathbf{u}$ is the velocity vector and $\underline{\underline{\tau}}$ is the stress tensor. The stress tensor relates the fluid stress to deformation. An expression that specifies $\underline{\underline{\tau}}$ is called constitutive equation. For an incompressible Newtonian fluid ($\nabla \cdot \mathbf{u} = 0$) the constitutive equation is given by [28]

$$\underline{\underline{\tau}} = -\mu \left[\nabla \mathbf{u} + (\nabla \mathbf{u})^T \right], \tag{2.3}$$

where μ is the dynamic viscosity. Expression (2.3) is also known as the (viscous) Newtonian constitutive equation and is often written in the form of

$$\underline{\underline{\tau}} = -\mu \underline{\underline{\dot{\gamma}}}, \tag{2.4}$$

where $\underline{\underline{\dot{\gamma}}}$ is the rate of strain tensor. Now substituting (2.3) into (2.1) and assuming that the only body force is due to surface tension yields

$$\rho \frac{D\mathbf{u}}{Dt} = -\nabla p + \mu \Delta \mathbf{u} + \mathbf{F}_{surf}, \tag{2.5}$$

Furthermore, the continuum equation for an incompressible fluid reduces to

$$\nabla \cdot \mathbf{u} = 0. \tag{2.6}$$

Equations (2.5) and (2.6) are known as the Navier-Stokes equations for an incompressible Newtonian fluid. A fluid is called non-Newtonian if it exhibits behavior that is not predicted by the Newtonian constitutive equation given by expression (2.3) [28].

2.2. Viscoelastic fluids

Rheology is the science of deformation and flow of all kinds of material [28]. An important step to accurately predict the fluid rheology is the formulation of a constitutive equation. Determining a constitutive equation for non-Newtonian fluid is a difficult challenge mainly because non-Newtonian fluids can behave differently over time when a certain stress or strain rate is applied. For example, when applying large shear rates, one fluid can exhibit shear-thinning, while the other fluid exhibits shear-thickening. Shear-thinning is characterized by a decreasing viscosity due to increased shear rates, while shear-thickening means an increasing viscosity when the shear rates are increased [28]. Viscosity is a measure of a fluid's resistance to flow. Furthermore, rheological properties can be time and temperature dependent. Apart from the (viscous) Newtonian constitutive equation, a constitutive equation for a purely linear elastic material is given by Hooke's law of elasticity [28]:

$$\underline{\underline{\tau}} = -G\underline{\underline{\gamma}}, \tag{2.7}$$

where G is the elastic modulus and $\underline{\underline{\gamma}}$ is the strain tensor. In this thesis, we will consider non-Newtonian fluids that can display both viscous and elastic behaviour[1], i.e. viscoelastic fluids. A way to measure the viscoelastic behaviour is by applying an oscillatory strain on the liquid and measuring the stress. For a purely elastic material, the stress and strain responses are in phase and for a purely viscous material, the strain will have a 90° phase shift. A viscoelastic material will have a delayed strain response in between that of 0° phase (purely elastic material) or a 90° phase shift (purely viscous material), see Figure 2.1. The viscous and elastic phase shifts can easily be deduced by using (2.4) and (2.7). That is, considering an oscillating stress in the form of a sine function, it then follows from (2.7) that the strain is proportional to the stress up to a constant for an elastic material which explains the zero phase shift between the responses. However, for a viscous material, the stress and strain are related by the derivative of the strain. The derivative of a sine function results in a cosine, hence a 90° phase shift.

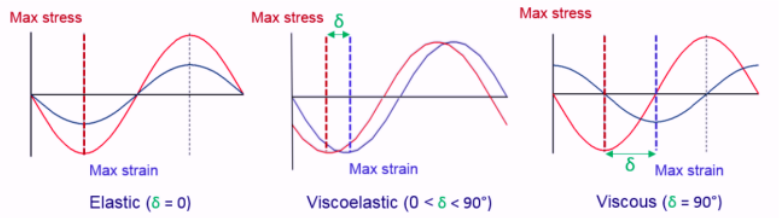

Figure 2.1: Stress and strain response for a purely elastic, purely viscous and a viscoelastic material, where δ is the phase shift [17].

The phase shift that determines the viscoelastic behaviour can be expressed in terms of the storage modulus G' and the loss modulus G'' by

$$\tan\delta = \frac{G''}{G'}. \tag{2.8}$$

Furthermore, for a sine changing shear strain[2], the stress response can be represented in terms of the storage and loss modulus:

$$\tau_{xy}(t) = \gamma_0 \left[G'(\omega)\sin\omega t + G''(\omega)\cos\omega t\right], \tag{2.9}$$

where ω is the frequency and γ_0 is the strain amplitude. For a full derivation, see Morrison [28].

2.3. Surface tension

In this section, based on Marchand et al. [23], we will explain surface tension from a macroscopic and a microscopic perspective. From a macroscopic view, surface tension is a restoring force expressed

[1] Note, that we consider the fluids only in its linear regime, i.e in the regime where the stress and strain have a linear relation.
[2] i.e. $\gamma(t) = \gamma_0 sin(\omega t)$.

as the force along an interface per unit length. The behaviour of surface tension is often described as membrane-like. We claim that the surface tension is a tangential force, to illustrate this we consider an U-shaped wire-frame, on which a sliding wire is attached, see Figure 2.2. The sliding occurs with negligible friction [23]. Between the frame and slider, there is a thin liquid film. By moving the slider, such that the film extends, we need a force **F** to keep the slider fixed. This force counteracts the contraction force due to the surface tension. The force **F** acts along the width of the thin film h, parallel to the the interface, which shows that the surface tension is a parallel force.

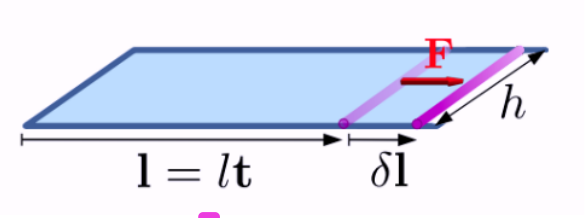

Figure 2.2: Experiment which shows that the surface tension is a force parallel to the interface [23].

From a microscopic perspective, surface tension occurs because molecules in the vicinity of an interface experience different forces then in the bulk. Considering a molecule in the bulk, we can see in Figure 2.3 (a) that the molecule is attracted equally in every direction. However, a molecule in the vicinity of an interface lacks half of the surrounding molecules, leading to an unbalance in the force. The strength of the surface tension is determined by the strength of the molecular bonds. We see that by only considering the attractive bonds, we would expect a net force perpendicular to the interface. However, from a macroscopic view we argued that the surface tension is a force parallel to the interface. The explanation why surface tension is a parallel force, consist of three parts: (i) explaining that the magnitude between the forces is different, (ii) explaining that attraction is anisotropic and repulsion is isotropic and (iii) discussing the effect of isotropic and anisotropic forces.

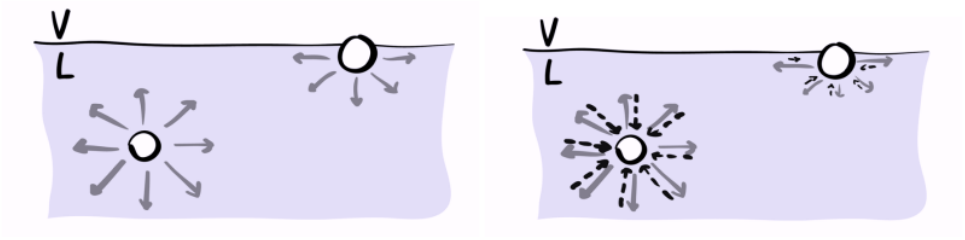

Figure 2.3: (a) Sketch of the attractive forces on molecules in a liquid, which shows the missing bonds at the interface, resulting in a nonzero net force. (b) A more complete sketch of the acting forces in the bulk and near the interface, where the gray arrows represent attractive forces and the dashed black arrows are negative forces [23].

(i) Explaining that the magnitude between the forces is different

Figure 2.3 (b) shows both the attractive and repulsive forces acting on a molecule. In the bulk we still observe a symmetry, which results in a net force of zero. However, near the interface the upward symmetry is broken. In order to have a vertical balance, the downward attractive force (gray arrow) should cancel the upward repulsive force (dashed arrow). For the direction, parallel to the interface, we observe that symmetry will be preserved, even near the interface. Therefore, the repulsive and attractive forces not necessarily balance each other. In general, the attractive forces are greater than the repulsive forces.

(ii) Explaining that attraction is anisotropic and repulsion is isotropic

We will now explain that not only the magnitudes differ, but that one force is isotropic and the other is not. We remark that repulsive forces are short ranged, while attractive forces are long ranged. Because of

the short range, repulsive forces are almost immune to changes in the surrounding molecule structure. We can therefore consider repulsive forces as isotropic. Now, since attractive forces are long ranged, they are highly dependent on the surrounding structure, making them anisotropic [23].

(iii) The effect of isotropic and anisotropic forces

We illustrate the effect of isotropic and anisotropic force through dividing the liquid into two subsystems with an imaginary boundary, parallel to the interface, see Figure 2.4. In Figure 2.4 (a) we have that the dotted subsystem is subjected to attractive (gray arrow) and repulsive (dashed black arrow) forces. We remark that the subsystem is in equilibrium, i.e. the attractive forces are in balance with the repulsive forces. Furthermore, the magnitude of the attractive forces increases, when moving away from the interface, due to an increasing density [23]. We will now consider an imaginary surface, perpendicular to the interface, see Figure 2.4 (b). We will now only consider forces in the direction parallel to the interface and remember that repulsive forces are isotropic. This means that the magnitude of the repulsive forces decreases near the interface, in a similar way as in Figure 2.4 (a). However, the attractive forces are long ranged and will hence remain almost constant, equal to the bulk attraction. We end up with a net force parallel to the surface, which has the greatest magnitude near the surface and vanishes in the bulk, see Figure 2.4 (c). Hence, resulting in a tangent surface tension force, parallel to the interface.

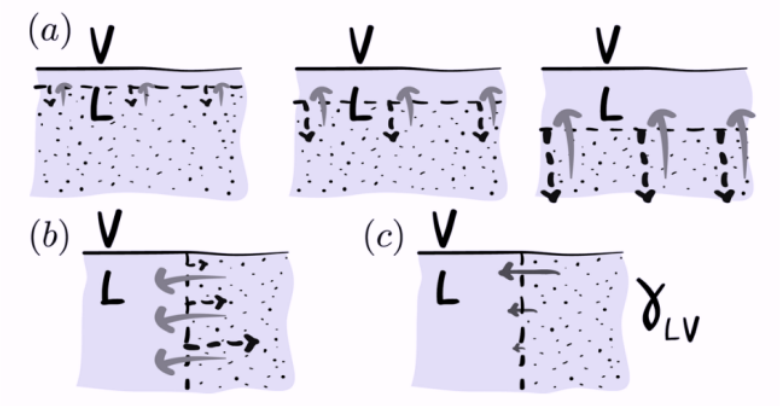

Figure 2.4: Forces acting on the dotted subsystem of the liquid by the not dotted subsystem. (a) We consider subsystems at different distances from the interface. The subsystems are subjected to a repulsive force (dashed black arrow) and an attractive force (gray arrow). The subsystems are in equilibrium. (b) We now consider subsystems with a boundary perpendicular to the interface. Since the attractive forces are anisotropic, they can be considered constant and equal to the bulk value. The negative forces are isotropic and should have, at equal distance from the interface, the same magnitude as in (a). (c) Resulting in a net force, parallel to the interface [23].

2.4. Balance: surface tension and pressure

In this section, we briefly explain the balance between the surface tension and the pressure. This balance will later on be used to determine the surface tension by measuring the pressure. For this we consider a droplet floating in air, where gravity forces are neglected. Furthermore, the fluid is assumed to be incompressible and the droplet is at rest. When only considering the surface tension, we have at the interface an imbalance in forces, see the previous section. Therefore, the surface tension wants to contract the droplet. However, due to incompressibility, a pressure force is created which counters the contraction. To better illustrate this, we cut the droplet into half, see Figure 2.5. We have that each half is at equilibrium, i.e. the net force is zero. From Figure 2.5, we see how a perpendicular pressure force balances a tangential surface tension force, due to a curved interface. This balance is expressed by the Young-Laplace equation [30]

$$\Delta P = \frac{2\sigma}{R}, \tag{2.10}$$

where ΔP is the pressure difference between inside and outside the droplet, σ is the surface tension and R the radius of the droplet.

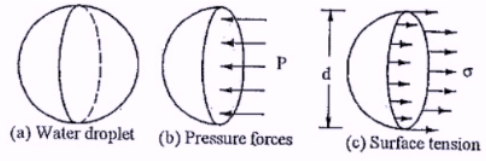

Figure 2.5: (a) The considered droplet, (b) the pressure forces acting on the half of the droplet and (c) the surface tension due to an imbalance at the interface. Image from `https://www.eeeguide.com/surface-tension/`

3

Smoothed Particle Hydrodynamics

In this chapter, based on the articles of Liu [22] and Hirschler et al. [13] we will first explain the basics behind SPH and discus the methods that are used to simulate an incompressible flow, namely Incompressible SPH (ISPH) and Weakly Compressible SPH (WCSPH). Furthermore, we will derive the SPH discretization of the incompressible Newtonian Navier-Stokes equations for both single-phase and multi-phase simulations. Then, we describe how we deal with the boundary conditions for WCSPH and ISPH simulations. Afterwards, we analyze the consistency of the numerical method and state the correction methods that will restore consistency. Finally, we explain the chosen kernel and conclude with stating the CFL conditions.

3.1. Basics SPH

In SPH the computational domain is represented by a finite set of particles where each particle carries the material properties. The interaction between the particles is controlled by a smoothing function; the smoothing function defines the mutual influence between particles based on their distance. However, we will first consider the smoothing function for a continuous field. The smoothing function is based on the following identity [22]:

$$f(\mathbf{r}) = \int_{\Omega} f(\mathbf{r}')\delta(\mathbf{r}-\mathbf{r}')d\mathbf{r}', \tag{3.1}$$

where $\mathbf{r}$ is the position vector and $\delta(\mathbf{r}-\mathbf{r}')$ is the Dirac delta function[1]. However, the delta function has only "one point" support and hence cannot be used to establish a discrete numerical model [22]. Now, replacing the Delta function with a smoothing function $W(r,h)$, we get the smoothed function approximation

$$f(\mathbf{r}) \approx \langle f(\mathbf{r})\rangle := \int_{\Omega} f(\mathbf{r}')W(\mathbf{r}-\mathbf{r}',h)d\mathbf{r}', \tag{3.2}$$

where h is the smoothing length, which is proportional to the radius of the kernel support domain Ω, see Figure 3.1 for an illustration of the smoothing function.

[1] The Dirac delta function is non-zero whenever $\mathbf{r}=\mathbf{r}'$ and everywhere else zero, furthermore $\int_{\Omega}\delta(\mathbf{r}-\mathbf{r}')d\mathbf{r}' = 1$.

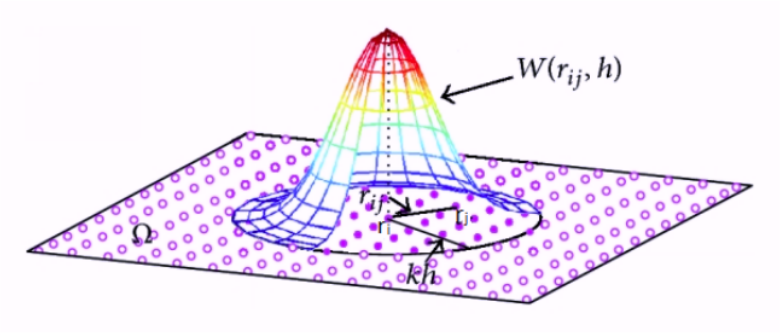

Figure 3.1: Illustration of a smoothed function/kernel in 2D, where r_i, r_j and r_{ij} are the particle of interest, neighbour particle and distance vector between the two particles [11].

For a function to be employed as an SPH smoothing function, the function needs to have the following properties [22]:

- Unity: $\int_\Omega W(\mathbf{r}-\mathbf{r}', h)d\mathbf{r}' = 1$.
- Compact support: outside of the supported domain the smoothing function should be equal to zero, that is
$$W(\mathbf{r}-\mathbf{r}', h) = 0, \text{ whenever } |\mathbf{r}-\mathbf{r}'| > \kappa h, \tag{3.3}$$
where κ is a scaling factor. Note: κh is called the cut-off radius and we define $q_{cut} := \kappa h$.
- Positivity: $W(\mathbf{r}-\mathbf{r}', h) \geq 0$ for any point in the domain.
- Decay: $W(\mathbf{r}-\mathbf{r}', h)$ decreases monotonously as $|\mathbf{r}-\mathbf{r}'|$ increases.
- Delta function approximation: $\lim_{h\to 0} W(\mathbf{r}-\mathbf{r}', h) = \delta(\mathbf{r}-\mathbf{r}')$, such that $< f(\mathbf{r}) >\to f(\mathbf{r})$.
- Symmetric property: smoothing function values for an equal distance size should be of equal value.

Properties and states such as density and velocity for the (discretized field) particles are calculated by an approximation of (3.2), that is

$$\langle f(\mathbf{r}_i)\rangle \approx \sum_{j=1}^{\mathcal{N}} f(\mathbf{r}_j)W(\mathbf{r}_i-\mathbf{r}_j,h)\Delta V_j = \sum_{j=1}^{\mathcal{N}} \frac{m_j}{\rho_j} f(\mathbf{r}_j)W(\mathbf{r}_i-\mathbf{r}_j,h), \tag{3.4}$$

where $\mathcal{N}$ is the total number of particles within the influence area of particle i, m_j is the corresponding mass of particle j, ρ_j is the density of particle j and ΔV_j is the volume occupied by particle j. In the last step of expression (3.4) we used that a volume without a fixed shape can be written as a mass to density ratio, that is $\Delta V_j = \frac{m_j}{\rho_j}$. Note that the gradient of the right hand side of (3.4) can be calculated exact by

$$\langle \nabla \cdot f(\mathbf{r}_i)\rangle \approx \sum_{j=1}^{\mathcal{N}} \frac{m_j}{\rho_j} f(\mathbf{r}_j)\cdot \nabla_i W(\mathbf{r}_i-\mathbf{r}_j,h). \tag{3.5}$$

For convenience, we will later on write $W(\mathbf{r}_i-\mathbf{r}_j,h)$ as W_{ij}. In the literature two different expressions for a particle derivative are used, which can be confusing and leads to wrong application of the expressions. The first expression is given in equation (3.5) and the second expression is given by

$$\langle \nabla \cdot f(\mathbf{r}_i)\rangle \approx -\sum_{j=1}^{\mathcal{N}} \frac{m_j}{\rho_j} f(\mathbf{r}_j)\cdot \nabla_j W_{ij}. \tag{3.6}$$

Observe that the first expression has a derivative taken with respect to particle i and the second expression has a derivative with respect to particle j. However, often in literature the notification with

which respect the derivative is taken is left out. The two expression are, however equivalent. To show this, first note that the derivatives can be expressed as

$$\nabla_i W(\mathbf{r}_i - \mathbf{r}_j, h) = W'(\mathbf{r}_i - \mathbf{r}_j, h)\frac{\partial(\mathbf{r}_i - \mathbf{r}_j)}{\partial \mathbf{r}_i} = W'(\mathbf{r}_i - \mathbf{r}_j, h)\frac{\mathbf{r}_i - \mathbf{r}_j}{|\mathbf{r}_i - \mathbf{r}_j|}, \tag{3.7}$$

and

$$\nabla_j W(\mathbf{r}_i - \mathbf{r}_j, h) = W'(\mathbf{r}_i - \mathbf{r}_j, h)\frac{\partial(\mathbf{r}_i - \mathbf{r}_j)}{\partial \mathbf{r}_j} = -W'(\mathbf{r}_i - \mathbf{r}_j, h)\frac{\mathbf{r}_i - \mathbf{r}_j}{|\mathbf{r}_i - \mathbf{r}_j|}, \tag{3.8}$$

resulting in $\nabla_i W(\mathbf{r}_i - \mathbf{r}_j, h) = -\nabla_j W(\mathbf{r}_i - \mathbf{r}_j, h)$. Both can be used, however a specific mention, with respect to which derivative is taken is needed.

3.2. Incompressible flow in SPH

When considering an incompressible flow, the solution methods can be divided into two classes, namely WCSPH and ISPH, where ISPH has gained increasing popularity in recent years. Two reasons for choosing ISPH over WCSPH are [4]:

- WCSPH requires a very short time step in order to enforce low compressibility, leading to large computational times.
- ISPH leads to a more accurate pressure representation.

However, a disadvantage of ISPH is the need for an additional boundary condition. In ISPH, the pressure is computed from a Pressure Poisson Equation (PPE), which requires pressure boundary conditions for some simulations this can lead to undesired problems. Therefore, in this study we perform both ISPH and WCSPH simulations. The main differences between WCSPH and ISPH is how they compute the pressure. WCSPH assumes a weakly-compressible fluid and calculates the pressure by an equation of state, which relates the density to pressure. We will first go into the details of ISPH, after which we discuss WCSPH.

3.2.1. ISPH

For an incompressible flow, we have an equivalent condition for the continuity equation (2.6), namely [15]

$$\nabla \cdot \mathbf{u} = 0 \iff \frac{d\rho}{dt} = 0. \tag{3.9}$$

The expressions are often referred to as divergence-free velocity (DV) and density-invariant (DI). Intuitively, we expect that to enforce incompressibility the best choice should be However, in Xu, Stansby, and Laurence [41] it was found that DV has a better accuracy than DI. In this study, we will only consider DV ISPH. ISPH method uses a predictor-corrector scheme in combination with a first-order Euler method in order to solve the incompressible DV Navier-Stokes equations. In the predictor step, the intermediate velocity (u^*) is calculated by solving the momentum equation excluding the pressure force, for a Newtonian fluid this yields [14]

$$\mathbf{u}_i^* = \mathbf{u}_i^n + \left(\mu \Delta \mathbf{u}_i^n + \mathbf{F}_{surf,i}^n\right)\frac{\Delta t}{\rho}, \tag{3.10}$$

where $\mathbf{u}_i^n$ is the particle velocity at the previous timestep. Note, that the particle position is not changed in the predictor step. In the corrector step the PPE is solved to enforce incompressiblilty

$$\nabla \cdot \left(\frac{1}{\rho}\nabla p^{n+1}\right)_i = \frac{\nabla \cdot \mathbf{u}_i^*}{\Delta t}. \tag{3.11}$$

After the above linear system is (iteratively) solved, the particle velocity and position (**r**) at the next time step are calculated by [14, 20, 6]

$$\mathbf{u}_i^{n+1} = \mathbf{u}_i^* - \left(\frac{1}{\rho}\nabla p^{n+1}\right)_i \Delta t \tag{3.12}$$

$$\mathbf{r}_i^{n+1} = \mathbf{r}_i^n + \left(\frac{\mathbf{u}_i^{n+1} + \mathbf{u}_i^n}{2}\right)\Delta t. \tag{3.13}$$

The ISPH method is implemented in the SPH software called "SiPER"[2]. In this software, the linear system given in (3.11) is solved using the algebraic multigrid preconditioner boomerAMG and a Bi-CGSTAB solver from the PETSc library [14, 13].

3.2.2. WCSPH

For WCSPH, the "weakly compressibility" is enforced on the fluid through an equation of state (EOS). We use the Tait equation, that is [13]

$$p - p_0 = \frac{\rho_0 c_o^2}{7}\left[\left(\frac{\rho}{\rho_0}\right)^7 - 1\right], \tag{3.14}$$

where ρ_0 is the reference density of the fluid and c_0 is the artificial speed of sound. c_0 determines how much the fluid is allowed to compress. In general, c_0 is chosen such that the fluid compressibility is limited to 1%, corresponding to a Mach number of 0.1 [27]. The Mach number is a dimensionless quantity that represents the ratio of the fluid velocity to the local speed of sound. In Morris, Fox, and Yi. [27] the following estimate for the value of c_0 is proposed

$$c_0^2 \sim \max\left(\frac{u^2}{\delta}, \frac{\mu u_{max}}{\rho L_0 \delta}, \frac{F_{surf} L_0}{\delta \rho}\right), \tag{3.15}$$

where

$$\delta = \frac{\Delta\rho}{\rho_0}. \tag{3.16}$$

Furthermore, L_0 is the initial particle distance, u_{max} is the maximum velocity and $\Delta\rho$ represent the maximum allowed density difference. From (3.14) we observe that the pressure will strongly respond to small variations in the density. A possible disadvantage is that small errors in the density lead to large errors in the pressure. However, the Tait equation is still one of the most commonly used EOS in the literature. In WCSPH, we can determine the density in two ways, namely by a particle summation or by the continuity equation. The former is done through using (3.4), that is

$$\rho_i = m_i \sum_{j=1}^{\mathcal{N}} W_{ij}, \tag{3.17}$$

and the latter involves the SPH discretization of the continuity equation (2.2) given by

$$\frac{d\rho_i}{dt} \approx \rho_i \sum_{j=1}^{\mathcal{N}} \frac{m_j}{\rho_j} \mathbf{v}_{ij} \cdot \nabla_i W_{ij}. \tag{3.18}$$

The advantage of (3.17) is that it conserves mass exactly in contrast to (3.18) [39]. We will therefore use (3.17). For the time integration, we use a simple first-order explicit scheme, namely forward Euler, which yields

$$\mathbf{u}_i^{n+1} = \mathbf{u}_i^n + \frac{\Delta t}{\rho}\left(\mu \Delta \mathbf{u}_i^n + \mathbf{F}_{surf,i}^n\right), \tag{3.19}$$

$$\mathbf{r}_i^{n+1} = \mathbf{r_i}^n + \frac{\Delta t^2}{\rho}\left(\mu \Delta \mathbf{u}_i^n + \mathbf{F}_{surf,i}^n\right), \tag{3.20}$$

where at each time step the pressure is determined by (3.14) and the density by (3.17)

3.3. SPH discretization

The discretization of the pressure term can be rewritten in many different forms, each with its advantages and disadvantages depending on the other discretization terms, the solver and if it is a single-phase or multi-phase simulation. We will first show why direct discretization is not often done in practice.

[2] SiPER is a program package from the University of Stuttgart. For more details see their website: `https://www.icvt.uni-stuttgart.de/en/research/siper/`.

Secondly, we will present the discretization terms for single-phase. After which, we will state the discretization terms for multi-phase. Direct discretization of the pressure term results in

$$\left(\frac{1}{\rho}\nabla p\right)_i \approx \frac{1}{\rho_i}\sum_{j=1}^{\mathcal{N}} \frac{m_j}{\rho_j} p_j \nabla_i W_{ij}. \tag{3.21}$$

To simplify the argument, we assume that the only acting force is the pressure force. Furthermore, note that we can express F_i as

$$F_i = m_i a_i,$$

and the pressure acceleration as

$$\frac{D\mathbf{u}_i}{Dt} = -\left(\frac{1}{\rho}\nabla p\right)_i. \tag{3.22}$$

Now, considering the force of particle i acting on particle j and vice versa, we observe that these forces are not symmetric, i.e.

$$F_i = -\frac{m_i m_j}{\rho_i \rho_j} p_j \nabla_i W_{ij} \neq -\frac{m_j m_i}{\rho_j \rho_i} p_i \nabla_j W_{ij} = \frac{m_j m_i}{\rho_j \rho_i} p_i \nabla_i W_{ij} = -F_j, \tag{3.23}$$

where the inequality follows from $p_i \neq p_j$. If we use direct discretization, we will no longer abide by the law of conservation of momentum. To solve this, the pressure term is first rewritten, after which the pressure term is discretized.

3.3.1. Single-phase

We will now derive the discretization for the pressure term. For this, we will first rewrite ∇p and then perform discretization. Because of this, we will end up with a symmetric term. Observe that ∇p can be rewritten as

$$\nabla p = \nabla p + p\nabla 1, \tag{3.24}$$

and we note that the SPH discretization of $\nabla 1$ is given by

$$\nabla 1 \approx \sum_{j=1}^{N} \frac{m_j}{\rho_j} \nabla_i W_{ij}. \tag{3.25}$$

Combining the above observations, we end up with the following symmetric pressure discretization

$$\frac{\nabla p}{\rho} \approx \sum_{j=1}^{N} \frac{m_j}{\rho_i \rho_j} \left(p_i + p_j\right) \nabla_i W_{ij}. \tag{3.26}$$

Secondly, we need to discretize the viscous term in the momentum equation (2.5), which is given by

$$\left(\frac{\mu}{\rho}\Delta \mathbf{u}\right)_i \approx \sum_{j=1}^{N} \frac{4m_j\left(\mu_i + \mu_j\right)}{\rho_j \rho_i} \left(\frac{\mathbf{r}_{ij}}{|\mathbf{r}_{ij}|^2} \cdot \nabla W_{ij}\right) \left(\mathbf{u}_i - \mathbf{u}_j\right). \tag{3.27}$$

The above discretizating involves complex steps and a correction term. These will be explained through the PPE discretizations. Due to the PPE, needed for ISPH, we have two additional discretizations terms, namely [14, 13]

$$\nabla \cdot \left(\frac{1}{\rho}\nabla p\right)_i \approx \sum_{j=1}^{N} \frac{m_j}{\rho_j} \frac{4}{\rho_j + \rho_i} \frac{p_{ij}\mathbf{r}_{ij}}{|\mathbf{r}_{ij}|^2} \cdot \nabla_i W_{ij}, \tag{3.28}$$

and

$$\left(\nabla \cdot \mathbf{u}^*\right)_i \approx \sum_{j=1}^{\mathcal{N}} \frac{m_j}{\rho_j} \left(\mathbf{u}^*{}_j - \mathbf{u}^*{}_i\right) \cdot \nabla_i W_{ij}, \tag{3.29}$$

where we introduced the abbreviation $\mathbf{r}_{ij} = \mathbf{r}_i - \mathbf{r}_j$. The derivation of the pressure force is based on the following integral approximant

$$\nabla \cdot \left(\frac{1}{\rho}\nabla p\right) \approx \int \left[\frac{1}{\rho(\mathbf{r}')} + \frac{1}{\rho(\mathbf{r})}\right] \left[p(\mathbf{r}) - p(\mathbf{r}')\right] \frac{(\mathbf{r} - \mathbf{r}') \cdot \nabla_r W_{rr'}}{|\mathbf{r} - \mathbf{r}'|^2} d\mathbf{r}'. \tag{3.30}$$

Using Taylor series about **r**, we can verify that the integral approximant is of second order accuracy [25][3]. The integral approximant in SPH form is

$$\nabla \cdot \left(\frac{1}{\rho}\nabla p\right)_i \approx \sum_{j=1}^{\mathcal{N}} \frac{m_j}{\rho_j}\left[\frac{1}{\rho_j}+\frac{1}{\rho_i}\right]\frac{p_{ij}\mathbf{r}_{ij}}{|\mathbf{r}_{ij}|^2}\cdot\nabla_i W_{ij}, \tag{3.31}$$

where $p_{ij} = p_i - p_j$. However, Cleary and Monaghan [7] showed that a correction term is needed, whenever the flux is discontinuous. The correction term is given by

$$\frac{4\frac{1}{\rho_i}\frac{1}{\rho_j}}{\frac{1}{\rho_i}+\frac{1}{\rho_j}}, \tag{3.32}$$

resulting in the final SPH discretization given in equation (3.28). Lastly, note that the SPH discretization of the intermediate velocity gradient in (3.29) is a result of rewriting with means of the product rule and applying basic SPH discretization.

3.3.2. Multi-phase

We use the multi-phase method presented in Adami, Hu, and Adams [2] suited for simulating density ratios. To account for the density discontinuities, the density of a particle i is determined by

$$\rho_i = m_i \sum_j W_{ij} = \frac{m_i}{V_i}. \tag{3.33}$$

In contrast to the general density approximation[4], (3.33) only affects the particle density i through the particle volume V_i, which permits a discontinuity in the density [2]. When the density is discontinuous, we have that $\frac{\nabla p}{\rho}$ is also discontinuous. To ensure continuity, we have to modify our current single-phase discretizations [15]. For the pressure gradient, we will use an average between the phases, that is [2]

$$\left(\frac{\nabla p}{\rho}\right)_i = \frac{1}{m_i}\left(\frac{m_i^2}{\rho_i^2}+\frac{m_j^2}{\rho_j^2}\right)\frac{p_i\rho_j + p_j\rho_i}{\rho_i+\rho_j}. \tag{3.34}$$

Furthermore, the multi-phase PPE is discretized as [15, 14]

$$\nabla \cdot \left(\frac{1}{\rho}\nabla p\right)_i \approx 2\frac{\rho_i}{m_i}\left(\frac{m_i^2}{\rho_i^2}+\frac{m_j^2}{\rho_j^2}\right)\frac{\nabla W_{ij}}{r_{ij}}\frac{p_{ij}}{\rho_i+\rho_j}, \tag{3.35}$$

and

$$(\nabla \cdot \mathbf{u})_i \approx \frac{\rho_i}{m_i}\sum_j \left(\frac{m_i^2}{\rho_i^2}+\frac{m_j^2}{\rho_j^2}\right)\overline{\mathbf{u}}_{ij}\nabla W_{ij}, \tag{3.36}$$

where $\overline{\mathbf{u}}_{ij}$ is the inter-particle average velocity given by

$$\overline{\mathbf{u}}_{ij} = \frac{\mu_i \mathbf{u}_i + \mu_j \mathbf{u}_j}{\mu_i + \mu_j}. \tag{3.37}$$

Expression (3.3.2) ensures continuity of the viscous force in case particle i and particle j belong to different phases with different viscosities [15].

3.4. Boundary conditions

Appropriate boundary conditions are needed to solve the Navier-Stokes equation. In this section, we will discuss solid walls and periodic boundary conditions. Furthermore, we will also address the needed pressure boundary for the PPE in ISPH. For a solid wall, the most obvious and important property is that no particles can penetrate through the wall. In literature, the most popular methods to implement solid walls are either by using ghost particles or mirror particles. The former simulates a solid wall by freezing

[3] For a more in depth derivation of the integral in multiple dimensions, see [25].
[4] $\rho_i = \sum_j m_j W_{ij}$.

multiple layers of particles. Depending on the type of wall (e.g. no-slip or free-slip) some properties of the frozen particles will change over time. For no-slip, the frozen particle velocity is equal to the inverted fluid particle velocity tangential to the boundary and scaled based on the distance between the two particles [14].

The latter approach, like the name suggests, will mirror the real fluid particles to the outside of the domain and will also mirror their properties. Based on the the type of wall, the velocity of mirrored particles will be altered. For a no-slip condition, the tangential velocity to the boundary is inverted. For free-slip, the velocity is equal to the real particle velocity [14]. The main advantage of ghost particles is the simplicity and stability to deal with curved boundaries. However, we will only make use of straight walls and in that case mirror particles are computational less expensive. This follows from that mirror particles are only used when a particle is close to the wall, reducing the run time [14]. Because of the computational advantage, we will use mirror particles.

We will now briefly discuss periodic boundaries conditions, but more details on the implementation requirements for periodic boundaries will be given in section 5.1. Periodic boundaries are much simpler than solid walls. It is often used to simulate an infinite domain. For periodic boundaries, the domain is replicated in the direction of periodic boundaries. That is, two boundaries are linked with each other and when a particle leaves the domain through a periodic boundary, it re-enters the domain at the corresponding boundary. Furthermore, particles near a periodic boundary are used in the kernel calculations for particles near the linked boundary [14][5]. Periodic boundaries are especially suited for WCSPH, since ISPH still needs a prescribed pressure value. For solid walls, we can set the pressure value of the mirror particles to zero, which corresponds to a zero Dirichlet pressure condition. However, for periodic boundaries, we will use a different method. But first, to better understand the need for a pressure value we note that the PPE has the following form

$$\mathbf{A} \cdot \mathbf{p}^{t+\Delta t} = \mathbf{b}, \tag{3.38}$$

where $\mathbf{A}$, $\mathbf{p}^{t+\Delta t}$ and $\mathbf{b}$ are the coefficient matrix, the unknown pressures and the divergences.

In order to have a unique solution, the matrix $\mathbf{A}$ should be nonsingular. For matrix $\mathbf{A}$ to be nonsingular, it suffices to use Dirichlet boundary conditions or fix the pressure for a single point [6]. We will make a distinction on how to deal with the singularity between multi-phase and free surface single-phase simulations.

For a multi-phase simulation, the coefficient matrix has diagonal components

$$A_{ii} = -2\frac{\rho_i}{m_i}\left(\frac{m_i^2}{\rho_i^2} + \frac{m_j^2}{\rho_j^2}\right)\frac{\nabla W_{ij}}{r_{ij}}\frac{1}{\rho_i + \rho_j}, \tag{3.39}$$

and the off-diagonal components

$$A_{ij} = 2\frac{\rho_i}{m_i}\left(\frac{m_i^2}{\rho_i^2} + \frac{m_j^2}{\rho_j^2}\right)\frac{\nabla W_{ij}}{r_{ij}}\frac{1}{\rho_i + \rho_j}. \tag{3.40}$$

To transform the singular matrix $\mathbf{A}$ in a nonsingular matrix, we fix the pressure at the corner points of the fluid[6]. We prescribe the pressure at the four corner points, in order to keep a symmetric system. We will enforce a zero pressure at the corner points, this is done by setting the diagonal component A_{cc} to minus one, the off-diagonal components A to zero and the divergence component b_c to zero[7].

For single-phase, we will prescribe a pressure in the form of a boundary condition at the free surface. However, the particles belonging to the free surface need to be first identified. This is done through the usage of a Shepard-kernel [13]:

$$S_i = \sum_{j=1}^{\mathcal{N}} \frac{m_j}{\rho_j} W_{ij}. \tag{3.41}$$

[5] A disadvantage of periodic boundaries is the current minimum requirement of 3 CPUS in the periodic direction, when doing parallel simulations. For a 2D simulation with only periodic boundaries, this requires at least 9 CPUS and for 3D it leads to at least 27 CPUS. Note, that the CPU demand is code specific. Additionally, when performing parallel simulations, we can not use periodic boundaries in the z-direction.

[6] In the SiPER code another way to deal with the singularity is to use the flag "KSP null space" from PETSc.

[7] The subscript c is the index of the corner points.

Due to a truncated kernel, the particles near the free surface will have a lower value. Particles with a value lower than 0.78 are labelled as free surface particles [13]. A natural boundary condition for free surface is a homogeneous Dirichlet boundary condition, i.e. $p = 0$. Due to the zero pressure condition, expression (3.28) yields

$$Cp_i \sum_j m_j \frac{4}{(\rho_i + \rho_j)^2} \frac{\mathbf{x}_{ij} \cdot \nabla W_{ij}}{\|\mathbf{x}_{ij}\|^2} = 0, \tag{3.42}$$

where C is an arbitrary constant. Enforcing a strict zero pressure boundary condition may lead to particle clustering or particles will start to drift apart [4]. Hence, it is preferable to impose "close" to zero pressure boundary conditions. This is done by adding (3.28) and (3.42) together, where C determines the weighting between satisfying zero pressure at the boundaries (3.42) and the regular PPE. In Hirschler et al. [13] a value of 2 is chosen for C, hence for a free surface particle, we replace the diagonal component of the coefficient matrix by

$$A_{ii} = -2 \sum_{j=1}^{\mathcal{N}} m_j \frac{4}{(\rho_i + \rho_j)^2} \frac{\mathbf{x}_{ij} \cdot \nabla W_{ij}}{\|\mathbf{x}_{ij}\|^2}, \tag{3.43}$$

and the off-diagonal components by

$$A_{ij} = \sum_{j=1}^{\mathcal{N}} m_j \frac{4}{(\rho_i + \rho_j)^2} \frac{\mathbf{x}_{ij} \cdot \nabla W_{ij}}{\|\mathbf{x}_{ij}\|^2}. \tag{3.44}$$

3.5. Kernel and particle consistency

The consistency of the SPH method depends on the kernel approximation and the particle approximation, where the order of consistency refers to which n'th order the numerical method can reproduce a polynomial exactly [22]. Using Taylor expansion the requirements for zero and first order consistency for the kernel approximation are given by [22][8]

$$\int_\Omega W(\mathbf{r} - \mathbf{r}', h) d\mathbf{r}' = 1, \tag{3.45}$$

$$\int_\Omega (\mathbf{r} - \mathbf{r}') W(\mathbf{r} - \mathbf{r}', h) d\mathbf{r}' = 0. \tag{3.46}$$

Observe that (3.45) and (3.46) are the unity and the symmetric properties of a smoothing function. Since, these properties are already satisfied, it can be concluded that the kernel approximation has up to C^1 consistency in regions without boundaries. For regions truncated with boundaries, the requirements (3.45) and (3.46) are not satisfied, according to lacking even C^0 consistency. In Figure 3.2, we observe that, due to boundary truncation, $W(\mathbf{r} - \mathbf{r}', h)$ is no longer an even function. As a result $(\mathbf{r} - \mathbf{r}') W(\mathbf{r} - \mathbf{r}', h)$ is no longer an odd function and when taking the integral the positive and negative parts no longer cancel each other out. Hence, (3.46) is not equal to zero resulting in the consistency requirements given by the Taylor expansion being violated.

By introducing a renormalization factor, C^0 consistency can be restored. Furthermore, with the usage of corrective kernels C^1 consistency for interior regions can be achieved. A 1D example of a corrective kernel approximation for a function $f(x)$ at particle i is given by [22][9]

$$f_i \approx \frac{\int f(x) W_i(x) dx}{\int W_i(x) dx}, \tag{3.48}$$

[8] Note achieving higher order consistency by solemnly relying on a smoothing function is impossible without violating the positivity requirement [22]. A smoothing function, which can be negative is undesirable, since it can result in unphysical solutions, such as negative density and negative energy.

[9] By Taylor expansion of $f(x)$ at a nearby point x_i and multiplying both sides with W and integrating over the entire computation domain, we get

$$\int f(x) W_i(x) dx = f_i \int W_i(x) dx + f_{i,x} \int (x - x_i) W_i(x) dx + \frac{f_{i,xx}}{2} \int (x - x_i)^2 W_i(x) dx + O(\Delta x)^3). \tag{3.47}$$

Combining expressions (3.47) and (3.48) the consistency statements about the correction kernel can be derived [22].

from where we can observe that for an interior region the corrective kernel has C^1 consistency and for a boundary region it has C^0 consistency, due to the normalization factor, which makes sure that equation (3.45) is satisfied.

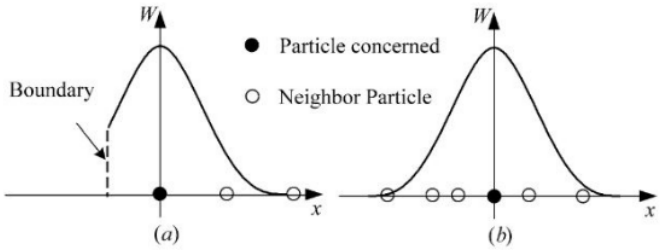

Figure 3.2: One-dimensional visual representation of the influence of a boundary (a) and particle disorder (b) on the consistency [22].

For the consistency of the particle approximation, we consider the discrete versions of (3.45) and (3.46)

$$\sum_{j=1}^{N} W(\mathbf{r}_i - \mathbf{r}_j, h)\Delta V_j = 1, \tag{3.49}$$

$$\sum_{j=1}^{N} (\mathbf{r}_i - \mathbf{r}_j)\, W(\mathbf{r}_i - \mathbf{r}_j, h)\Delta V_j = 0. \tag{3.50}$$

In general, C^0 consistency is not achieved, since requirement (3.49) is violated due to particle disorder or truncation of the support domain by boundaries. A way to restore C^0 consistency is by renormalization [22]. In Di G. Sigalotti et al. [9] the requirement for C^2 consistency is derived[10], that is

$$\langle x^2 \rangle - \langle x \rangle^2 = 0, \tag{3.51}$$

where $\langle\,\rangle$ is the kernel approximation. Expression (3.51) is only achieved when $N \to \infty$, $h \to 0$, and $\mathcal{N} \to \infty$, with $\mathcal{N}$ the number of particles within the kernel support and N the total number of particles. A common mistake in SPH to increase the resolution is to keep $\mathcal{N}$ fixed while letting $N \to \infty$ and $h \to 0$. By doing this a residual error will not vanish. The residual error will only vanish when we abide by the following scaling [9]

$$\mathcal{N} \propto N^{\frac{1}{2}}. \tag{3.52}$$

However, the increase in kernel particles, whenever the total number of particles increases, demands the use of a Wendland-type kernel [33]. The reason behind this is that when $\mathcal{N}$ attains large values, standard SPH smoothing kernels become unstable due to particle clumping. A Wendland-type kernel avoids particle clumping for all values of $\mathcal{N}$ [8][11]. Furthermore, an error bound for the SPH estimate of a function is given in Sigalotti et al. [33]. We refer to Sigalotti et al. [33] for the expression and derivation of the error bound. Furthermore Sigalotti et al. [33] concluded that the particle approximation converges to the kernel approximation independently of h, when the following scaling is satisfied[12]

$$\mathcal{N} \propto h^{n-\beta}, \tag{3.53}$$

where n is the spatial dimension and $\beta > n$. In 3D, $\beta \in [5, 7]$, where a low value for β means that the particles are orderly distributed and a high value stands for a random particle distribution. By combining (3.52) and (3.53), we obtain a family of possible scaling describing the dependence of $\mathcal{N}$ and h on N [33].

[10] Provided that C^0 and C^1 consistency is already satisfied. Furthermore the requirement is derived in the 1D case, but can be extended to higher dimensions.

[11] This follows from a linear stability analysis performed by Dehnen and Aly [8]. Dehnen and Aly [8] conclude that smoothing kernels whose Fourier transform is negative will inevitably trigger pairing instability for large enough $\mathcal{N}$. Wendland kernels have been constructed with the condition that they need to posses a non-negative Fourier transform.

[12] When $\mathcal{N} \to \infty$, we need to have that the particle mass scales with h as $m \propto h^{\beta}$, with $\beta < n$. This results in the requirement that $m \to 0$ as $h \to 0$, which leads to the scaling $\mathcal{N} \propto h^{n-\beta}$ [33].

3.6. Kernel type

An important factor in determining the stability, efficiency and the accuracy of the SPH solution is the choice of the kernel. In the literature, we can find a lot of different kernels. However, throughout this thesis, we will use a Wendland C2 kernel, see (3.54) [18]. The main reason for choosing a Wendland-type kernel is the earlier mentioned immunity to particle clumping. Furthermore, from a comparison with different kernels (Cubic spline, Gauss and Quintic kernels) it followed that the Wendland-type kernel has the best "ability" to obtain the highest accuracy [32].

$$W\left(\mathbf{r}_{ij},h\right)=\alpha_d\begin{cases}\left(1-\frac{q}{2}\right)^4\left(2q+1\right) & 0\leq q\leq 2\\ 0 & 2<q\end{cases}, \tag{3.54}$$

where $q=\frac{|\mathbf{r}_{ij}|}{h}$ and α_d is a scaling factor to ensure unity for different spatial dimensions. For 1D, 2D and 3D, the corresponding values for α_d are $\frac{3}{4h}$, $\frac{7}{4\pi h^2}$ and $\frac{21}{16\pi h^3}$. We note that we can express the compact radius q_{cut} as two times the smoothing length h. We have seen that for discretizing a spatial derivative of a function the first derivative of the kernel is needed. The first derivative of the considered kernel is given by

$$\frac{\partial W\left(\mathbf{r}_{ij},h\right)}{\partial \mathbf{r}_{ij}}=\alpha_d\begin{cases}-\frac{5q}{h}\left(1-\frac{q}{2}\right)^3 & \text{if } 0\leq q<<2\\ 0 & 2<q\end{cases}. \tag{3.55}$$

Figure 3.3 shows the 1D Wendland C2 kernel and its first derivative, where the smoothing lenght is set to $h=1\ m$. From Figure 3.3, we observe the earlier mentioned properties of the kernel, such as symmetry, positivity, decay and compact support.

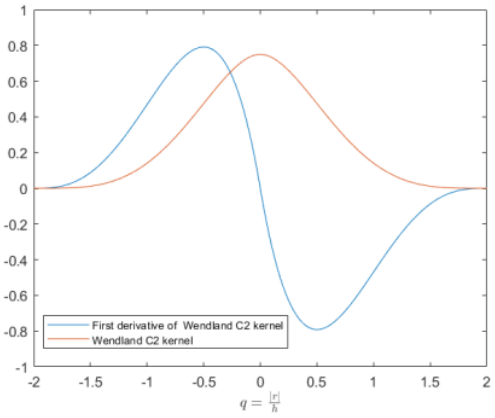

Figure 3.3: One dimensional Wendland C2 kernel and its first derivative, where $h=1\ m$.

3.7. Correction methods

In section 3.5, we saw that SPH without corrections can have consistency problems. This is especially the case for free surface simulations, since there the kernel will be truncated at the free surface. In this section, we will elaborate on two correction methods that will restore the consistency, namely particle shifting and the correction method from by Bonet and Lok.

3.7.1. Particle shifting

Particle shifting is used to prevent particle disordering and voids from occurring. The particles are shifted after a full time-step, where the particle properties such as the velocity will be corrected using a Taylor expansion. This puts a limit on the maximum shifting distance. The maximum shifting distance depends on the maximum velocity, timestep and the smoothing length. The particle shift is given by [13, 41]

$$\delta\mathbf{r}_i=C\alpha\mathbf{R}_i, \tag{3.56}$$

where α is the shifting magnitude which is equal to $u_{max}dt$, $\mathbf{R}_i$ is the shifting vector and C is a constant, with a value between 0.01 and 0.1, depending on the required stability and accuracy. The shifting magnitude is given by

$$\mathbf{R}_i = \sum_{j=1}^{\mathcal{N}} \frac{\bar{r}_i^2}{r_{ij}^2} \mathbf{n}_{ij} \tag{3.57}$$

where $\mathbf{n}_{ij}$ is the unit distance vector between particles i and j and $\bar{r}_i$ is the average particle distance, given by

$$\bar{r}_i = \frac{1}{\mathcal{N}} \sum_{j=1}^{\mathcal{N}} r_{ij}. \tag{3.58}$$

For more details we refer to Hirschler et al. [13].

3.7.2. Bonet and Lok correction

In the literature, we can find a lot of different corrections. Some will adjust the gradient, whereas others will modify the kernel itself. Also, combinations of these methods are proposed. A popular correction method is the mixed gradient and kernel correction from Bonet and Lok [5]. Like the name suggest, it is a combination of a gradient and a kernel correction. The kernel correction is chosen such that the consistency conditions in (3.49) and (3.50) are satisfied. This is done by a weighted average or equivalently Shepard-kernel. The correction kernel is given by [5]

$$\tilde{W}_{ij} = \frac{W_{ij}}{\sum_{j=1}^{\mathcal{N}} \frac{m_j}{\rho_j} W_{ij}} = \frac{W_{ij}}{S_i}. \tag{3.59}$$

As an example, the density at particle i can now be determined by

$$\rho_i = \sum_{j=1}^{\mathcal{N}} m_j \tilde{W}_{ij}. \tag{3.60}$$

The gradient correction is determined in such a way that it will preserve angular momentum, this is done by satisfying the following condition [5]

$$\sum_{j=1}^{\mathcal{N}} \frac{m_j}{\rho_j} (\mathbf{r}_j - \mathbf{r}_i) \otimes \nabla_i W_{ij} = \mathbf{I}, \tag{3.61}$$

where $\mathbf{I}$ is the Identity matrix. We will satisfy the above condition by introducing a correction matrix $\mathbf{L}$, which leads to the following corrected gradient

$$\tilde{\nabla}_i \tilde{W}_{ij} = \mathbf{L}_i \nabla_i W_{ij}, \tag{3.62}$$

where $\mathbf{L}_i$ is obtained by satisfying (3.61), yielding

$$\mathbf{L}_i = \left(\sum_{j=1}^{\mathcal{N}} \frac{m_j}{\rho_j} (\mathbf{r}_j - \mathbf{r}_i) \otimes \nabla_i W_{ij} \right)^{-1}. \tag{3.63}$$

Noteworthy is that we will approximate all gradients with the corrected gradient of the kernel. However, we will not replace all kernels with the corrected kernels. This is because sometimes the uncorrected kernel gives better results. For example, it was found that using the uncorrected density in the PPE yields a better performance [10].

3.8. CFL-conditions

We will now state the Courant-Friedrichs-Lewy criterion (CFL) which is a necessary condition to guarantee a stable simulation. The limited time step for ISPH is given by

$$\Delta t = min\left(\Delta t_u, \Delta t_{visc}, \Delta t_a, \Delta t_\sigma\right), \tag{3.64}$$

where Δt_u, Δt_{visc}, Δt_a and $\Delta t\sigma$ are given by

$$\begin{aligned}\Delta t_u &= \alpha_{CFL}\frac{L_0}{u_{max}}\\ \Delta t_{visc} &= \alpha_{diff}\frac{L_0^2}{\nu_{max}}\\ \Delta t_a &= \alpha_{diff}\sqrt{\frac{L_0}{|a_{max}|}}\\ \Delta t_\sigma &= \alpha_{diff}\frac{L_0^3\rho}{2\pi\sigma},\end{aligned} \tag{3.65}$$

with $\alpha_{CFL} = 0.05$, L_0 the initial particle distance, u_{max} is the magnitude of the maximum velocity, a_{max} is the magnitude of the maximum acceleration, $\alpha_{diff} = 0.125$, ν_{max} the maximum kinematic viscosity [13] and σ the surface tension coefficient. For WCSPH, to enforce a limit on the compressibility of the fluid, the maximum velocity criterion is changed to

$$\Delta t_v = \alpha_{CFL}\frac{L_0}{c_0}, \tag{3.66}$$

Depending on the limiting timestep criterion, WCPSH can have a much smaller time step than ISPH. At the end of every time step, a check is performed. Whenever a criterion has been violated, the last time step will be repeated with a smaller time step.

4

Rheology and surface tension in SPH

In this section, we will first explain how the rheological properties are implemented. Furthermore, we will derive an expression that can estimate the effect of the PIF on the surface tension and the pressure. Lastly, we will describe two methods that can be used to simulate the surface tension, namely Continuum Surface Force (CSF) and Particle Interaction Surface Minimization Force (PISMF).

4.1. Tuning of rheological fluid properties

In Van der Linde [40] it has been shown that PIF can be used to tune rheological properties of the simulated fluid. The rheological PIF introduces an additional force, that generates an attraction for distant particles and repulsion for close particles. There are multiple ways to express and implement PIF. We will implement PIF as a force, instead of an acceleration force, which was done in Van der Linde [40]. The SPH discretization of the momentum equation (2.5) including the PIF is given by [39]

$$\frac{D\left(m_i \mathbf{u}_i\right)}{Dt} = \mathbf{F}_i^p + \mathbf{F}_i^\mu + \mathbf{F}_i^{int}, \tag{4.1}$$

where $\mathbf{F}_i^p$ and $\mathbf{F}_i^\mu$ are the SPH discretizations of the pressure gradient and viscous forces and $\mathbf{F}_i^{int}$ is the total PIF acting on particle i. For the considered rheological PIF from Van der Linde [40], the total interaction force is given by

$$\mathbf{F}_i^{int} = -\sum_{j=1}^{\mathcal{N}} F_{ij} \frac{\mathbf{r}_{ij}}{r_{ij}}, \tag{4.2}$$

where F_{ij} is

$$F_{ij} = \begin{cases} m_j \frac{S_{ij}}{w} \left(-\left(r_{ij} - k\right)^2 + w \right), \; k = \frac{x_1^2 - x_2^2}{2x_1 - 2x_2}, \; w = (x_2 - k)^2, & r_{ij} \leq x_2 \\ 0, & r_{ij} > x_2. \end{cases} \tag{4.3}$$

The tunable parameters are the interaction strength (S_{ij}), the range of the particle interaction (x_2) and the ratio of repulsive/attractive force (x_1). The visual representation of equation 4.3 is given in Figure (4.1).

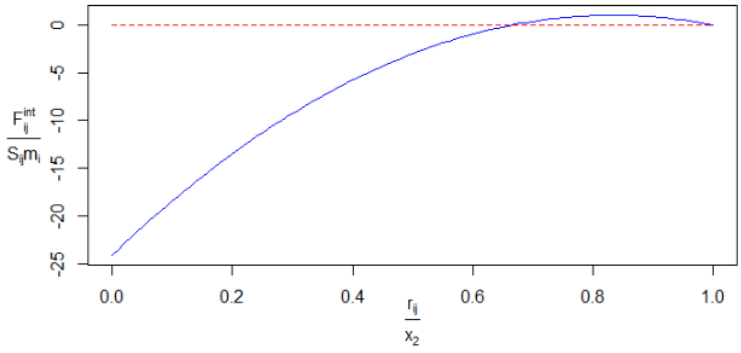

Figure 4.1: Visual representation of the particle interaction force (blue) given by equation 4.3, where on the horizontal axis we have the normalized distance and on the vertical axis we have the normalized force. Furthermore, the red dashed line represents the zero line and the first interception between the red and blue line is determined by x_1.

We will now state the side effects due to the PIF. The first known side effect is an additional pressure due to a difference in the amount of repulsive and attractive forces [40, 39]. The additional pressure will from now on be referred to as the virial pressure. Secondly, the PIF affect the surface tension.

For a 2D simulation, we can measure the viral pressure by the following expression [21]

$$p_{virial} = \frac{1}{2V}\left\langle \sum_i \sum_j \mathbf{r}_{ij} \cdot \mathbf{F}_{ij} \right\rangle, \tag{4.4}$$

where $\langle \cdots \rangle$ denotes the average over time and $\mathbf{F}_{ij} = F_{ij}\frac{\mathbf{r}_{ij}}{r_{ij}}$. However, it would be better if we can estimate beforehand the virial pressure and effect on the surface tension.

4.2. Analytical estimate surface tension and virial pressure

We will now derive an 2D analytical expression for the PIF induced virial pressure and surface tension. In the beginning, the derivation procedures for the surface tension and the pressure coincides. At a certain point we will mention that from there on, the derivations will differ from each other. At that point, we will continue with the derivation for the surface tension after which we will do the final derivation steps for the virial pressure. We will follow the derivation of Tartakovsky and Panchenko [39], which was done for multi-phase fluids and we will make the necessary changes needed for a free surface fluid.

The total stress at a point **x** can be found according to Hardy's formula as the sum of the convection stress and the interaction stress [39]. Now, considering a static equilibrium, the total stress reduces to the interaction stress. The interaction stress due to PIF is given by [39]

$$\mathbf{T}_{int}(\mathbf{x}) = \frac{1}{2}\sum_{i=1}^{N}\sum_{j=1}^{N} \mathbf{f}_{ij} \otimes (\mathbf{r}_j - \mathbf{r}_i) \int_0^1 \tilde{\psi}_\eta (\mathbf{x} - s\mathbf{r}_i - (1-s)\mathbf{r}_j)\, ds, \tag{4.5}$$

where $\mathbf{f}_{ij}$ is the total force between particle i and particle j and $\tilde{\psi}_\eta$ is a weighting function with compact support. Note that the force $\mathbf{f}_{ij}$ can be written as [39]

$$\mathbf{f}_{ij} = \phi_{\alpha\beta}(r_{ij})\frac{\mathbf{r}_{ij}}{r_{ij}}, \tag{4.6}$$

where α, β indicates the different phases[1] and

$$\phi_{\alpha\beta}(r_{ij}) = -\left[F_{\alpha\beta}^{P} + F_{\alpha\beta}^{int}\right]. \tag{4.7}$$

[1] For free surface, we will only have one phase, namely α.

We remark that $F^P_{\alpha\beta}$ depends on the choice of the pressure discretization. We use the following discretization

$$F^P_{\alpha\beta} = (\frac{p_\alpha + p_\beta}{\rho_\alpha \rho_\beta}) \frac{dW(z)}{dz}. \tag{4.8}$$

Furthermore, $\tilde{\psi}_\eta$ is given as a product of one-dimensional compact functions $\psi_{\eta,l} = \frac{1}{\eta}\psi(\mathbf{x}(l))$, where $l = 1, 2, 3$ denotes the vector component [39].

We consider a single fluid α, with a flat free surface parallel to the x direction[2]. Without loss of generality we set the free surface at $y = 0$ and fluid α occupies the domain $\mathcal{I} = -\infty < x < \infty, -\infty < y < 0$. The surface tension is then determined by integrating the stress components along the interface, that is [39]

$$\sigma = \int_{-\infty}^{0} [T_\tau(y) - T_n(y)]\, dy, \tag{4.9}$$

where $T_\tau(y)$ and $T_n(y)$ are the tangent and normal stress components. Using (4.5) we write T_τ as

$$T_\tau(\mathbf{x}) = -\frac{1}{2} \sum_{i\in\mathcal{I}} \sum_{j\in\mathcal{I}} \phi\left(r_{ij}\right) \frac{\left(\mathbf{r}_{ij(x)}\right)^2}{r_{ij}} \int_0^1 \tilde{\psi}_\eta \left(\mathbf{x} - (s\mathbf{r}_i + (1-s)\mathbf{r}_j)\right) ds, \tag{4.10}$$

where $\mathbf{r}_{ij(x)}$ is the x component of the vector $\mathbf{r}_{ij}$. We assume that the radial distribution function is equal to one, i.e. the particles are homogeneous distributed. By approximating the sums with integrals we get

$$T_\tau(\mathbf{x}) \approx -\frac{1}{2} n^2 \int_{\mathcal{I}} \int_{\mathcal{I}} \phi\left(r_{ij}\right) \frac{\left(\mathbf{r}_{ij(x)}\right)^2}{r_{ij}} \int_0^1 \tilde{\psi}_\eta \left(\mathbf{x} - (s\mathbf{r}' + (1-s)\mathbf{r}')\right) ds d\mathbf{r}' \mathbf{r}'', \tag{4.11}$$

where n is the numerical density, i.e. $n = \frac{\rho}{m}$. We introduce the following notation

$$\begin{aligned} &\mathbf{r}' = (x', y'), \quad \mathbf{r}'' = (x'', y''), \\ &\boldsymbol{\rho} = \mathbf{r}' - \mathbf{r}'' = (\rho_1, \rho_2), \\ &\mathbf{R} = \tfrac{1}{2}(\mathbf{r}' + \mathbf{r}'') = (R_1, R_2), \end{aligned} \tag{4.12}$$

which will later on be used to simplify equations. Next, we rewrite (4.11) as[3]

$$\begin{aligned} T_\tau(\mathbf{x}) = -\frac{1}{2} n_1^2 \int_{-\infty}^{\infty} \int_{-\infty}^{0} \int_{-\infty}^{\infty} \int_{-\infty}^{0} \phi\left(|\mathbf{r}' - \mathbf{r}''|\right) \frac{(x' - x'')^2}{|\mathbf{r}' - \mathbf{r}''|} \\ \times \int_0^1 \tilde{\psi}_\eta \left(\mathbf{x} - (s\mathbf{r}' + (1-s)\mathbf{r}'')\right) ds dy'' dx'' dy' dx'. \end{aligned} \tag{4.13}$$

Following the same steps, T_n is given by

$$\begin{aligned} T_n(\mathbf{x}) = -\frac{1}{2} n_1^2 \int_{-\infty}^{\infty} \int_{-\infty}^{0} \int_{-\infty}^{\infty} \int_{-\infty}^{0} \phi\left(|\mathbf{r}' - \mathbf{r}''|\right) \frac{(y' - y'')^2}{|\mathbf{r}' - \mathbf{r}''|} \\ \times \int_0^1 \tilde{\psi}_\eta \left(\mathbf{x} - (s\mathbf{r}' + (1-s)\mathbf{r}'')\right) ds dy'' dx'' dy' dx'. \end{aligned} \tag{4.14}$$

Since we are considering a square domain, we can factorise our compact function as

$$\tilde{\psi}_\eta(\mathbf{x}) = \psi_\eta(x)\psi_\eta(y), \tag{4.15}$$

where ψ is chosen to be a step-wise function and is normalized in the following way

$$\psi_\eta(x) = \frac{1}{\eta}\psi\left(\frac{x}{\eta}\right), \quad \psi(x) = \begin{cases} 1 & \text{if } x \in (-1/2, 1/2), \\ 0 & \text{otherwise,} \end{cases} \tag{4.16}$$

[2] To apply for curved free surfaces, the following assumption needs to be satisfied: the radius of the curvature needs to be much larger than the smoothing length.

[3] Remember that we consider a square fluid with domain $-\infty < x', x'' < \infty$ and $-\infty < y', y'' < 0$.

and

$$\Psi_\eta(y_1,y_2,R_2)=\int_{y_1}^{y_2}\psi_\eta(y-R_2)\,dy=\begin{cases}0 & \text{if } R_2<y_1-\frac{1}{2}\eta,\\ \frac{1}{\eta}\left(-y_1+R_2+\frac{1}{2}\eta\right) & \text{if } y_1-\frac{1}{2}\eta\le R_2<y_1+\frac{1}{2}\eta,\\ 1 & \text{if } y_1+\frac{1}{2}\eta\le R_2<z_2-\frac{1}{2}\eta,\\ \frac{1}{\eta}\left(y_2-R_2+\frac{1}{2}\eta\right) & \text{if } y_2-\frac{1}{2}\eta\le R_2<y_2+\frac{1}{2}\eta,\\ 0 & \text{if } R_2\ge y_2+\frac{1}{2}\eta.\end{cases}\tag{4.17}$$

Observe that when both points are inside the compact radius Ψ_η has the value one, when both points are outside we have zero and between we have a linear trend.

By using the factorisation, we rewrite the expression inside the last integral of (4.13) as

$$\tilde{\psi}_\eta\left(\mathbf{x}-(s\mathbf{r}'+(1-s)\mathbf{r}'')\right)=\psi_\eta\left(x-(sx'+(1-s)x'')\right)\psi_\eta\left(y-(sy'+(1-s)y'')\right),\tag{4.18}$$

and by approximating the integral by the midpoint value we get

$$\begin{aligned}&\int_0^1\tilde{\psi}_\eta(\mathbf{x}-(s\mathbf{r}'-(1-s)\mathbf{r}''))\,ds=\int_0^1\psi_\eta(x-(sx'+(1-s)x''))\psi_\eta(y-(sy'+(1-s)y''))ds\\ &\approx\psi_\eta(x-(\frac{1}{2}x'+(1-\frac{1}{2})x''))\psi_\eta(y-(\frac{1}{2}y'+(1-\frac{1}{2})y'')).\end{aligned}\tag{4.19}$$

Now inserting the above derived expression into (4.13) and (4.14) and subtracting we have

$$\begin{aligned}T_\tau-T_n\approx-\frac{1}{2}n^2\int_{-\infty}^{\infty}\int_{-\infty}^{0}\int_{-\infty}^{\infty}\int_{-\infty}^{0}&\phi\left(|\mathbf{r}'-\mathbf{r}''|\right)\frac{(x'-x'')^2-(y'-y'')^2}{|\mathbf{r}'-\mathbf{r}''|}\\ &\times\psi_\eta(x-(\frac{1}{2}x'+(1-\frac{1}{2})x''))\psi_\eta(y-(\frac{1}{2}y'+(1-\frac{1}{2})y''))dy''dx''dy'dx'.\end{aligned}\tag{4.20}$$

Changing the variables of integration from $\boldsymbol{r}',\boldsymbol{r}''$ to $\boldsymbol{\rho},\boldsymbol{R}$ and taking into account that the Jacobian matrix is equal to one, we get

$$T_\tau-T_n\approx-\frac{1}{2}n^2\int_{-\infty}^{\infty}\int_{-\infty}^{0}\int_{-\infty}^{\infty}\int_{2R_2}^{-2R_2}\phi(|\boldsymbol{\rho}|)\frac{\rho_1^2-\rho_2^2}{|\boldsymbol{\rho}|}\psi_\eta\left(x-R_1\right)\psi_\eta\left(y-R_2\right)d\rho_2d\rho_1dR_2dR_1.\tag{4.21}$$

The integration bounds of ρ_2 follow from $y'=R_2+\frac{1}{2}\rho_2<0$, and $y''=R_2-\frac{1}{2}\rho_2<0$, i.e. when we first integrate with respect to ρ_2, we have to take into account that ρ_2 is bounded between $2R_2$ and $-2R_2$, which follows from the considered y-domain $(-\infty,0)$.

In the next step, we observe, that integrating with respect to R_1 allows us to make use of the normalization condition of ψ_η, i.e.

$$\int_{-\infty}^{\infty}\psi_\eta(x-R_1)dR_1=1.\tag{4.22}$$

To justify switching the order of integration, we use Fubini's theorem, that is for a chosen ϕ the absolute value of the quadruple integral should be finite[4]. Assuming that changing the order of integration is justified we obtain

$$T_\tau-T_n\approx\frac{1}{2}n^2\int_{-\infty}^{0}\int_{-\infty}^{\infty}\int_{2R_2}^{-2R_2}\phi(|\boldsymbol{\rho}|)\frac{\rho_1^2-\rho_2^2}{|\boldsymbol{\rho}|}\psi_\eta\left(y-R_2\right)d\rho_2d\rho_1dR_2.\tag{4.23}$$

Because of the absolute value, we have that $\phi(|\boldsymbol{\rho}|)$ is a symmetric function. Secondly, we observe the symmetric integral bounds of ρ_1 and ρ_2 and thirdly the integral depends only on another symmetric function $\frac{\rho_1^2-\rho^2}{|\boldsymbol{\rho}|}$. Using the above observations, we can rewrite (4.23) as

$$T_\tau-T_n\approx2n^2\int_{-\infty}^{0}\int_{0}^{\infty}\int_{0}^{-2R_2}\phi(|\boldsymbol{\rho}|)\frac{\rho_1^2-\rho_2^2}{|\boldsymbol{\rho}|}\psi_\eta\left(y-R_2\right)d\rho_2d\rho_1dR_2.\tag{4.24}$$

[4] ϕ is assumed to be a continuous function. When an explicit expression for ϕ is chosen, we have to verify if the absolute value of the quadruple integral is finite.

We will again perform a change of variables, but now changing ρ_1, ρ_2 to polar coordinates t, ξ. For the bounds we note that due to the x domain t takes values between zero and infinity. If $t \in (0, -2R_2)$, then ξ takes values between 0 and $\frac{\pi}{2}$ while, if $t \in (-2R_2, \infty)$, ξ takes values between 0 and $\hat{\xi}$, where $\hat{\xi} = \sin^{-1}(-\frac{2R_2}{t})$. Furthermore, taking the extra t into account due to the Jacobian and that

$$\frac{\rho_1^2 - \rho_2^2}{|\boldsymbol{\rho}|} = t\cos(2\xi),$$

we get

$$\begin{aligned} T_\tau - T_n \approx &- 2n^2 \int_{-\infty}^{0}\int_{0}^{-2R_2}\int_{0}^{\frac{\pi}{2}} \phi(t)t^2 \cos(2\xi)\psi_\eta\left(y - R_2\right) d\xi dt dR_2 \\ &- 2n^2 \int_{-\infty}^{0}\int_{-2R_2}^{\infty}\int_{0}^{\hat{\xi}} \phi(t)t^2 \cos(2\xi)\psi_\eta\left(y - R_2\right) d\xi dt dR_2. \end{aligned} \tag{4.25}$$

From here on out the derivation steps for the surface tension and the pressure will differ. Continuing with the derivation for the surface tension we first perform the integration with respect to ξ, that is

$$T_\tau - T_n \approx -n^2 \int_{-\infty}^{0}\int_{-2R_2}^{\infty} \phi(t)t^2 \sin(2\hat{\xi})\psi_\eta\left(y - R_2\right) dt dR_2. \tag{4.26}$$

Substituting the above expression into (4.9) and first performing the integration with respect to y yields

$$\begin{aligned} \sigma = \int_{y_1}^{y_2} T_\tau - T_n dy &\approx \int_{y_1}^{y_2} -n^2 \int_{-\infty}^{0}\int_{-2R_2}^{\infty} \phi(t)t^2 \sin(2\hat{\xi})\psi_\eta\left(y - R_2\right) dt dR_2 dy \\ &= -n^2 \int_{-\infty}^{0}\int_{-2R_2}^{\infty} \phi(t)t^2 \sin(2\hat{\xi}) dt dR_2. \end{aligned} \tag{4.27}$$

For the final step we want to change the order of integration. We observe that we can describe the integration region

$$\begin{aligned} &-\infty < R_2 < 0 \\ &-2R_2 < t < \infty, \end{aligned} \tag{4.28}$$

for the $dtdR_2$ integral, also by

$$\begin{aligned} &0 < t < \infty \\ &-\frac{1}{2}t < R_2 < 0, \end{aligned} \tag{4.29}$$

which is the description needed for the integration order $dR_2 dt$. Now changing the order of integration and performing the integration we end up with

$$\begin{aligned} \sigma &\approx -n^2 \int_{-\infty}^{0}\int_{-2R_2}^{\infty} \phi(t)t^2 \sin(2\hat{\xi}) dt dR_2, \\ &= -n^2 \int_{0}^{\infty}\int_{-\frac{1}{2}t}^{0} \phi(t)t^2 \sin(2\hat{\xi}) dR_2 dt, \\ &= -\frac{1}{3}n^2 \int_{0}^{\infty} \phi(t)t^3 dt. \end{aligned} \tag{4.30}$$

We will now derive the induced virial pressure in the bulk of the fluid. In the bulk far away from the free surface the pressure is given by [39]

$$p = -T_\tau = -T_n. \tag{4.31}$$

By starting with (4.11) and performing the same steps up to (4.25) we get

$$\begin{aligned} p = -T_\tau \approx &2n^2 \int_{-\infty}^{0}\int_{0}^{-2R_2}\int_{0}^{\frac{\pi}{2}} \phi(t)t^2 \cos^2(\xi)\psi_\eta\left(y - R_2\right) d\xi dt dR_2 \\ &+ 2n^2 \int_{-\infty}^{0}\int_{-2R_2}^{\infty}\int_{0}^{\hat{\xi}} \phi(t)t^2 \cos^2(\xi)\psi_\eta\left(y - R_2\right) d\xi dt dR_2. \end{aligned} \tag{4.32}$$

To simplify the above expression, we choose a negative y with large $|y|$ such that the support of $\psi_\eta(y - R_2)$ falls inside the interval $(-\infty, 0)$. Because of this, the estimated virial pressure can only be used to predict the pressure in the bulk of the fluid, i.e. far away from the interface. Using that the range of $\phi(t)$ is finite, we can move y further from the interface, to ensure that $\phi(t) = 0$ for all $t > -2R_2$. By doing this the second triple integral becomes zero and we can extend the integration in t to $(0, \infty)$, yielding

$$p \approx 2n^2 \int_{-\infty}^{0} \int_{0}^{\infty} \int_{0}^{\frac{\pi}{2}} \phi(t) t^2 \cos^2(\xi) \psi_\eta \left(y - R_2\right) d\xi dt dR_2. \tag{4.33}$$

We remark that by our assumption the support of $\psi_\eta \left(y - R_2\right)$ lies inside the integration interval of R_2. This integral is equal to one because of the normalization property of ψ_η. As the last step, we perform the integration with respect to ξ, which results in the final expression for the pressure in terms of the unknown interaction function ϕ, that is[5]

$$p \approx \frac{1}{2}\pi n^2 \int_{0}^{\infty} \phi(t) t^2 dt. \tag{4.34}$$

To obtain a clear overview of the previous calculations, we state the final expressions for the PIF induced surface tension and virial pressure

$$\begin{aligned} \sigma_{PIF} &\approx -\frac{1}{3} n^2 \int_{0}^{\infty} \phi(t) t^3 dt, \\ p_v &\approx \frac{1}{2}\pi n^2 \int_{0}^{\infty} \phi(t) t^2 dt. \end{aligned} \tag{4.35}$$

Two methods are considered for further tuning of the surface tension, namely the Continuum Surface Force (CSF) method and a particle interaction surface minimization force (PISMF) method. Both methods are based on a force that minimises the surface area. We will first discus the CSF method after which the PISMF method will be explained.

4.3. Continuum surface force method

One of the biggest advantages of CSF is that it does not influence the viscosity or elasticity of the fluid. The CSF method translates the surface tension into a volumetric force. The force acts as a smoothing for high curvature regions in order to minimize the surface area. The volumetric force is given by [14, 26]

$$\mathbf{F}_{surf} = \sigma \kappa \hat{\mathbf{n}} \delta_s, \tag{4.36}$$

where σ is the surface tension coefficient, $\hat{\mathbf{n}}$ the unit surface normal, κ is the curvature and δ_s is the surface delta function. We have assumed that the surface tension is constant throughout the fluid, i.e. $\nabla_s \sigma = 0$, where ∇_s is the surface gradient. In order to distinguish between different phases and determine the normal and curvature, we introduce a color function c as [2]

$$c_l^k = \begin{cases} 1, & \text{if particle } l \text{ belongs to } k, \\ 0, & \text{else.} \end{cases} \tag{4.37}$$

With the color function, we can now obtain the unit normal using [14]

$$\hat{\mathbf{n}} = \frac{\nabla c}{[c]}, \tag{4.38}$$

where $[c]$ is the colour jump across the interface. Furthermore, using (4.37) the curvature is given by [14]

$$\kappa = -\nabla \cdot \hat{\mathbf{n}}. \tag{4.39}$$

For the surface delta function, we will use the same expression as in Hirschler et al. [14]

$$\delta_s = |\mathbf{n}|, \tag{4.40}$$

[5] We have changed the order of integration. Like before, when an expression for ϕ is assumed, the absolute value of the triple integral should be computed and needs to be finite.

where $|\mathbf{n}|$ denotes the length of the normal vector. Before we give the discretization of the unit normal and the curvature, we will briefly discuss the shortcomings of CSF. To overcome the shortcomings, we state different solutions found in the literature, each with its own advantages and disadvantages.

The drawbacks of the CSF method are that the accuracy depends on the normal vector calculation and curvature estimation, where the later is prone to errors. To resolve the error prone calculations of the curvature, many corrections were introduced, each with its own pros and cons. In Adami and Account [1] a comparison of the most popular correction methods is presented. From the comparison, it followed that the classical method developed by Sirotkin and Yoh [34] is the most stable one. They used a correction matrix to solve the problem of the decreased number of interpolation points near the free surface for one-fluid phases, resulting in more accurate results. Furthermore, a transition band (multiple layers of surface particles) for the calculation of the curvature is introduced. Other methods, such as presented by [2] and [26] tend to underestimate the curvature near the surface. However, stability still remains to be an issue, since it will depend on many other factors such as the pressure force, order of viscosity force and the density calculation near the free surface.

Despite all the corrections, the methods are still depending on the amount of particles; the methods become less reliable when handling thin liquid layers with few particles. He et al. [12] developed another method that is able to handle thin film features. The difference between the methods is that He et al. [12] uses $|\nabla c|^2$ instead of ∇c, with the advantage that the normal direction is no longer needed, which causes high errors in thin film sheets. This turns out to improve robustness against particle sparsity.

For stability reasons, we will base our discretization on the classical method from Sirotkin and Yoh [34], which is also used in Hirschler et al. [13]. For the discretization of the unit normal and the curvature, we make a distinction between multi-phase and single-phase. For multi-phase, the discretization terms are

$$\mathbf{n}_i = \sum_{j=1}^{\mathcal{N}} \frac{m_j}{\rho_j} (c_j - c_i) \tilde{\nabla}_i \tilde{W}_{ij}, \tag{4.41}$$

and

$$\kappa_i = \sum_{j=1}^{\mathcal{N}} \frac{m_j}{\rho_j} (\hat{\mathbf{n}}_i - \hat{\mathbf{n}}_j) \tilde{\nabla}_i \tilde{W}^n_{ij}, \tag{4.42}$$

where $\tilde{\nabla}_i \tilde{W}^n_{ij}$ denotes the usual corrected gradient, see section 3.7.2. However, now only particles with a normal vector length $|\mathbf{n}| > \frac{0.01}{h}$ are considered [14]. For single-phase, the normal vector reduces to

$$\mathbf{n}_i = \sum_{j=1}^{\mathcal{N}} \frac{m_j}{\rho_j} c_j \tilde{\nabla}_i \tilde{W}_{ij}. \tag{4.43}$$

Furthermore, for single-phase, we perform a smoothing on the normal and curvature to ensure a smooth field, i.e. [13, 10]

$$\tilde{\mathbf{n}}_i = \frac{\sum_{j=1}^{\mathcal{N}} \mathbf{n}_j W_{ij}}{\sum_{j=1}^{\mathcal{N}} W_{ij}}, \tag{4.44}$$

and

$$\tilde{\kappa}_i = \frac{\sum_{j=1}^{\mathcal{N}} \kappa_j W_{ij}}{\sum_{j=1}^{\mathcal{N}} W_{ij}}. \tag{4.45}$$

Finally, the surface tension for a multi-phase particle i is given by

$$\mathbf{F}_{surf,i} = \sigma_i \kappa_i |\mathbf{n}_i| \hat{\mathbf{n}}_i, \tag{4.46}$$

and for single-phase by

$$\mathbf{F}_{surf,i} = \sigma_i \tilde{\kappa}_i |\mathbf{n}_i| \hat{\tilde{\mathbf{n}}}_i. \tag{4.47}$$

4.4. Particle interaction surface minimization force

The PISMF method was first introduced as a complementary force to PIF, where the PIF was designed with the purpose to simulate the surface tension. Examples of such PIF are Tartakovsky and

Panchenko [39] and Akinci, Akinci, and Teschner [3]. The first step of the PISMF method is to compute the normal vector based on the gradient of the density field [3, 16]

$$\mathbf{n}_i = h \sum_{j=1}^{\mathcal{N}} \frac{m_j}{\rho_j} \nabla_i W(|\mathbf{r}_{ij}|), \tag{4.48}$$

where h is the smoothing length. To give an expression for the minimization force, we use the assumption that the magnitude of $\mathbf{n}_i$ is proportional to the curvature. The minimization force is then given by

$$\mathbf{F}_i^{curv} = -\gamma m_i \sum_{j=1}^{\mathcal{N}} (\mathbf{n}_i - \mathbf{n}_j), \tag{4.49}$$

where γ is a coefficient to control the strength of the surface tension. It can be easily verified that $\mathbf{F}_i^{curv}$ increases, whenever the curvature increases. Furthermore, for flat regions and inside the fluid, the force is equal to zero. This is exactly what we wanted. The force should only influence the surface area and must act as a minimization. The particle surface force is then given by

$$\mathbf{F}_i^{surf} = K_i \left(\mathbf{F}_i^{int} + \mathbf{F}_i^{curv} \right), \tag{4.50}$$

where

$$K_i = \sum_{j=1}^{\mathcal{N}} \frac{2\rho_0}{\rho_i + \rho_j}, \tag{4.51}$$

is a symmetrized correction factor, with ρ_0 the initial density of the fluid. The advantages of the PISMF method are

- Avoids explicit computation of the surface curvature. Hence, improving sensitivity to particle disorder.
- Avoids normalization of $\mathbf{n}_i$.
- Symmetric force.

However, an important remark of PISMF is that it requires a PIF that is designed to simulate a surface tension force. The disadvantage of this is that it will affect the rheological properties, which leads to a coupling between the surface tension and the fluid rheology. The goal of this study is to tune the surface tension to the desired value, without affect the rheology. Therefore, in this study, we will not use PISMF and only use CSF.

5

Problem description

In this section, we will first describe the general SPH simulation setup. Afterwards we will state two ways that will be used to measure the surface tension, where the first one is valid for both Newtonian and non-Newtonian fluids and the second one is only valid for low viscosities.

5.1. Simulation details

The desired fluid will be simulated in a box (partly) filled with fluid particles. The particles will be initialized on a grid, where the particle placement is defined in terms of the (initial) particle diameter L_0. The particle diameter is defined by

$$L_0 = \frac{L_x}{N_{particles}}, \tag{5.1}$$

where L_x is the length of the box in the x-direction (meters) and $N_{particles}$ is the maximum possible number of particles in the x-direction[1], see Figure 5.1. The particles can now be placed on the grid by expressing the coordinates x, y and z in terms of L_0. Important to note is that when $L_x = L_y$ and the maximum number of particles in the y-direction is larger than in the x-direction, the particles will cram/merge together.

For periodic boundaries of the box, the box is extended in every direction through attaching a copy of the whole box at every border, see Figure 5.2. Due to the periodic box, conditions should be met to prevent computational errors. These conditions are:

- The kernel cut-off distance should be smaller than the dimensions of the box divided by two.
- When a particle leaves the box at a certain boundary, the particle should enter the box at the opposite boundary.

The first restriction follows from the fact that due to the periodic box, particles can interact not only with other particles in the central box, but also with the "copied" particles. To avoid errors, a particle should only be allowed to interact with one instance of any other particle; either being it in the same box or a periodic image of it. This results in the restriction on the cut-off distance, see Figure 5.2.

[1] L_0 is solemnly based on the x-direction.

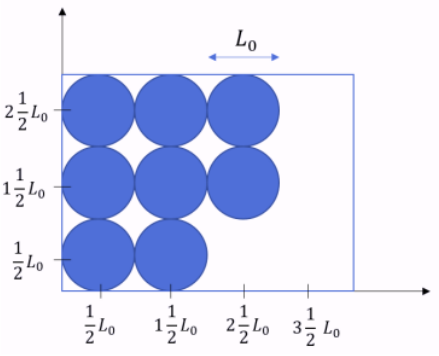

Figure 5.1: Visualisation of initial particle placement in 2D. When we take $L_x = 2\ m$, we have that $L_0 = \frac{1}{2}\ m$, since the maximum number of particles is equal to 4.

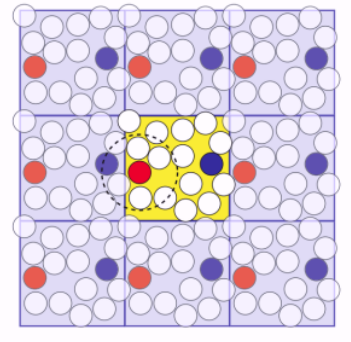

Figure 5.2: Example of a 2D periodic box, where the dashed line indicates the cut-off radius of the red particle and the yellow box represents the central box. Observe, that if the cut-off distance is increased, the red particle will interact with multiple blue particles [30].

5.2. Numerical methods to measure the surface tension

The first method to measure the surface tension involves the deformation of an initially square droplet. The surface tension acts as a minimization of the droplet surface, which transforms the square droplet into a circular droplet, see Figure 5.3. When the droplet reaches a stationary state, the surface tension is in equilibrium with the pressure difference at the interface of the droplet. Using the Young-Laplace equation, this balance is expressed as [21]

$$P_{in} - P_{out} = \frac{\sigma}{R}, \tag{5.2}$$

where R is the equilibrium radius of the droplet and P_{in} and P_{out} are the pressure inside and outside the droplet. We will validate the numerical method by computing the difference between the calculated and the expected surface tension. Additionally, this method is used to determine the PIF influence on the surface tension.

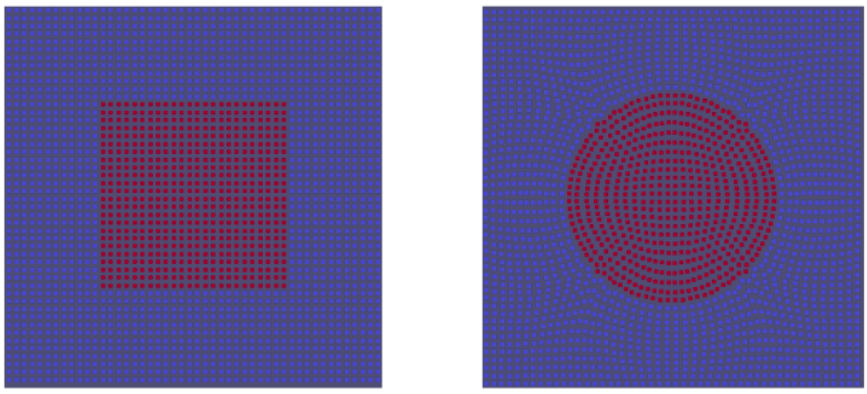

(a) (b)

Figure 5.3: Visualization of the particle positions at the initial time (a) and at the end of the simulation (b). The red particles represent the inner fluid and the blue particles represent the outer fluid.

For the second method, we will measure the surface tension in a dynamic setting. The second method simulates an oscillating droplet with small-amplitudes and low viscosity. We will describe two methods that will be used to initialize the oscillation. For the first method, we start with a circular droplet

with a prescribed divergence-free initial velocity field [37]

$$u_x = u_0 \frac{x}{r_0}\left(1 - \frac{y^2}{r_0 r}\right) exp\left(-\frac{r}{r_0}\right), \tag{5.3}$$

$$u_y = -u_0 \frac{y}{r_0}\left(1 - \frac{x^2}{r_0 r}\right) exp\left(-\frac{r}{r_0}\right), \tag{5.4}$$

where u_0 determines the strength of the velocity field, $r_0 = 0.25R$ and r the distance from the position (x, y) to the droplet center. For positive u_0, the droplet will stretch out in the x-axis and compress in the y-axis. The second method starts with an initial droplet in the shape of an ellipse.

Because of the surface tension, the droplet wants to return to its original circular form. This is done in an oscillating way. The theoretical period is given by [21]

$$T = 2\pi R \sqrt{\frac{R(\rho_d + \rho_l)}{6\sigma}}, \tag{5.5}$$

where ρ_d and ρ_l are the droplets density and the surrounding density. To determine the period, we use the position of the center of mass of the droplet's upper right quarter. The center of mass of the whole droplet is given by

$$\mathbf{R}_d = \frac{\sum_{i \in \Omega_d} m_i \mathbf{r}_i}{\sum_{\Omega_d} m_i}, \tag{5.6}$$

where Ω_d represent particles belonging to the inner fluid. In a similar way, the upper right center of mass is given by

$$\mathbf{R}_{ur} = \frac{\sum_{i \in \Omega_{ur}} m_i \mathbf{r}_i}{\sum_{\Omega_{ur}} m_i}, \tag{5.7}$$

where Ω_{ur} represent particles belonging to the upper right quarter of the inner fluid.

6

Results and discussion

In this chapter, we will first validate the CSF method for free surfaces. Secondly, we do the same for multi-phase simulations. Then, we will verify the estimates for the PIF. Lastly, we will state the main findings of this thesis, namely the results when CSF and PIF are combined.

6.1. Free surface simulations

In order to validate the numerical method, we will simulate a (free surface) square droplet, which will transform into a circular state due to surface tension, see section 5.2 for more details. The surface tension is implemented with the CSF method. We only consider an ISPH solver in combination with periodic boundaries and prescribing "close" to zero pressure boundary conditions, see section 3.4. Furthermore, we use the correction methods described in section 3.7. The numerical parameters are

- ρ = $1.0\ \frac{kg}{m^3}$.
- Number of particles = 61×61.
- $\mu = 0.2\ Pa \cdot s$.
- $\sigma = 1\ \frac{N}{m}$.
- Dimensions box = $0.6 \times 0.6\ m$.
- q_{cut} = $4.2\ L_0$.

Figure 6.1 shows that the droplet reaches a circular state. However, what cannot be seen in Figure 6.1 is that the droplet starts to develop linear momentum, i.e. the droplet will start to move trough the box. This behaviour is also observed by Fürstenau, Weißenfels, and Wriggers [10]. Furthermore, during the simulations numerical instabilities are observed, see Figure 6.2. In Fürstenau, Weißenfels, and Wriggers [10] a possible explanation for the observed linear momentum and the instabilities is because of the absence of strict Dirichlet boundary conditions, which makes the problem ill posed, see section 3.4. We remark that by increasing the viscosity, the instabilities can be delayed. Another way to solve the instabilities is by introducing an outer fluid. The outer fluid will act as a stabilizer. By introducing a second layer the computational time will drastically increase. However, since our goal is to combine CSF with PIF and this combination can result in additional unforeseen instabilities, we choose stability over efficiency. Hence, we switch to multi-phase simulations.

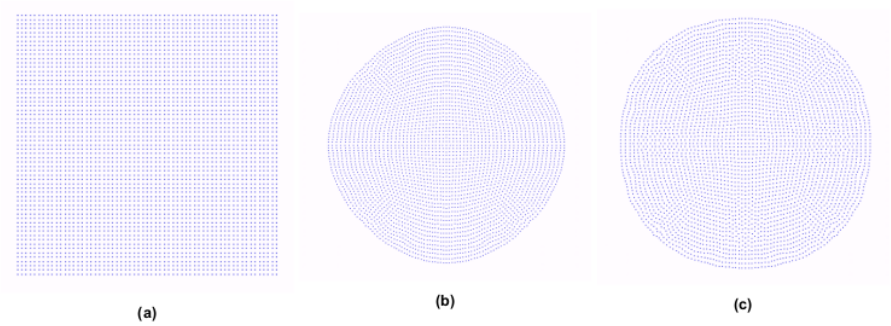

Figure 6.1: (a) Initial square droplet at rest, (b) the evolved droplet due to surface tension at t = 0.4 s and (c) the circular state at t = 1 s.

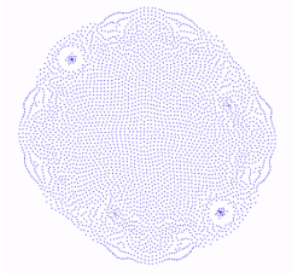

Figure 6.2: Representation of the instability which occurs when μ is changed from $0.2\ Pas$ to $0.02\ Pas$.

6.2. Multi-phase simulations

This section will first present the results for the deformation benchmark test. After which, the results for the oscillating droplet will be presented and discussed.

6.2.1. Droplet deformation: benchmark

The first method to verify the implementation is by considering an initially square droplet, which deforms due to the surface tension. We will use the same parameters as in [2, 15, 28] in order to make a comparison between the results. The inside droplet has an initial size of $0.6 \times 0.6\ m$ and is placed inside the center of the outer fluid, with length and width of $1 \times 1\ m$. The parameters of both fluids is set to ($\rho = 1\ \frac{kg}{m^3}, \mu = 0.2\ Pa \cdot s, \sigma = 1\ \frac{N}{m}$), which corresponds to [2, 15, 28]. Furthermore, the total number of particles N is 100×100 and the cut-off length q_{cut} is set to four times the initial particle distance. Additionally, the particle shifting method and the correction kernels and gradients are used, see section 3.7.

Figure 6.3 (a) shows the pressure distribution at final time $t = 5\ s$. We observe a constant pressure profile inside and outside the droplet and spikes at interface between the two fluids. These spikes also occurred in the results of Szewc, Pozorski, and Minier [36] and Adami, Hu, and Adams [2].

To calculate the average surface tension, based on Laplace law, only particles with a Shepard value greater than 0.99 are considered. The mean surface tension over time is shown in Figure 6.3 (b), with a maximum relative error of 2.1 %.

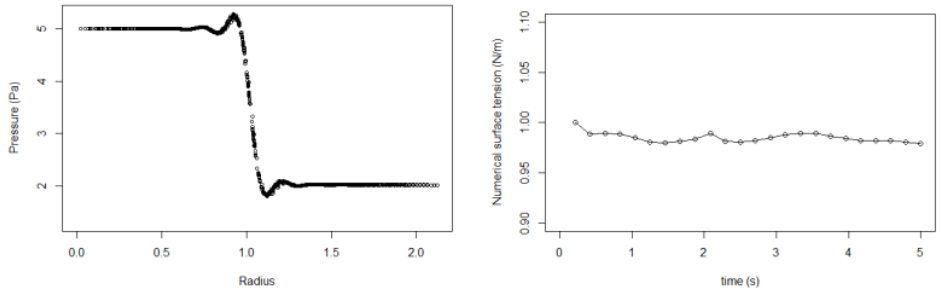

(a) (b)

Figure 6.3: Pressure profile of the inside and outside fluid at final time $t = 5\ s$ (a) and the numerical surface tension plotted against time (b).

6.2.2. Oscillating droplet: benchmark

For the oscillating droplet we consider two problems. The first problem is an oscillating droplet, where the density and the viscosity between the outer and inner fluid are equal, i.e. $\rho_d = \rho_l = 1.0\ \frac{kg}{m^3}$ and $\mu_d = \mu_l = 0.05\ Pa \cdot s$. The second problem involves an oscillating droplet with a density ratio $\frac{\rho_l}{\rho_d} = 0.001$ and a viscosity ratio $\frac{\mu_l}{\mu_d} = 0.01$. A realistic example of a density ratio of 0.001 is a water droplet suspended in the air. For the first problem, we will make a comparison between our results and the results of Adami, Hu, and Adams [2]. The second problem mimics the oscillation of a free droplet. For free surface droplets we know the analytical period (expression (5.5)). We will validate the code by computing the relative error between the numerical and the analytical period. We again only consider the ISPH solver.

In Figure 6.4, we visualize the particle positions at four different time instances and Figure 6.5 (a) shows the oscillation of the centre of mass of the droplet's upper right quarter, with no density/viscosity ratio. By a visual comparison with Adami, Hu, and Adams [2] we observe a relative good agreement between our results and their higher resolution results ($N = 14400$). It is worth mentioning here that the results of Adami, Hu, and Adams [2] show a larger difference between calculated periods for different resolutions. Additionally, our results contain fewer fluctuations. Possible reasons are different solvers[1] and different discretizations terms for the normal and curvature calculations.

Figure 6.5 (b) shows a comparison between the numerical and the analytical period, with the previously specified density and viscosity ratio. The simulation parameters are: $N = 60 \times 60$, an initial equal particle distance, $\sigma = 1\ N/m$ and an initial radius of $0.2\ m$. We observe a good agreement between the numerical and analytical period, with a maximum relative error of 1.9 %, see Table 6.1. The periods are based on the intersections, where we ignore the starting points.

[1] Their simulations were performed with a WCSPH solver and our simulations are performed with an ISPH solver.

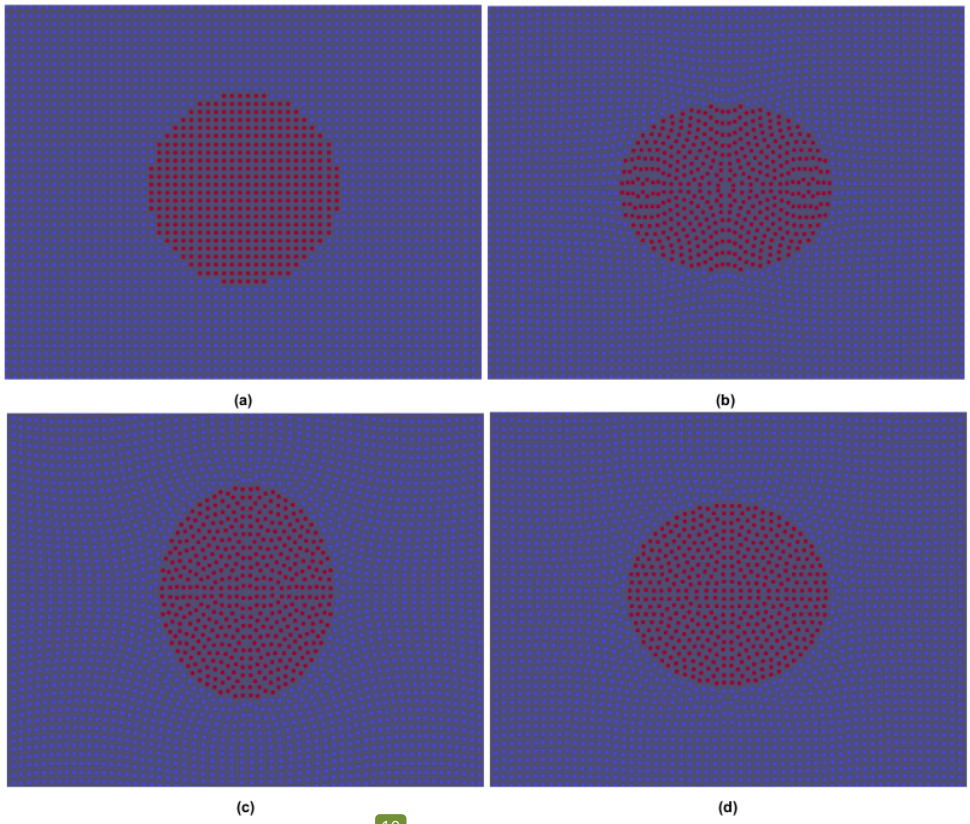

Figure 6.4: Droplet oscillation at different time instances, namely t=0.0, 0.1, 0,3 and 0.5 s.

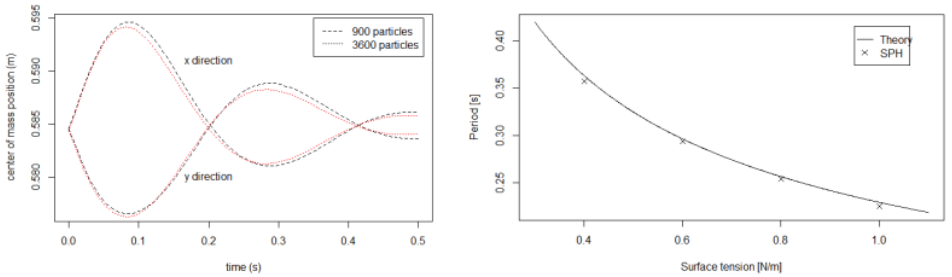

(a) (b)

Figure 6.5: Droplet oscillation with equal density and viscosity, i.e. $\rho_d = \rho_l = 1$ and $\mu_d = \mu_l = 0.05$ (a). Comparison of period between the numerical and the theoretical results with $\frac{\rho_l}{\rho_d} = 0.001$ and $\frac{\mu_l}{\mu_d} = 0.01$(b).

σ_{CSF}	Theoretical period	Measured period	Relative error
0.4	0.3625	0.357	0.016
0.6	0.2962	0.294	0.0089
0.8	0.2565	0.254	0.0090
1.0	0.2294	0.225	0.019

Table 6.1: The calculated values for the measured and estimate Period, with $\frac{\rho_l}{\rho_d} = 0.001$ and $\frac{\mu_l}{\mu_d} = 0.01$.

6.3. Verification of analytical estimation

In this section we first validate the analytical estimation with the deformation test (single-phase). Secondly, repeat the same test but now for multi-phase. After which we perform the oscillating droplet test.

6.3.1. Droplet deformation: analytical estimation

To validate the code and the analytical estimate (4.35) we will use the pairwise forces of Tartakovsky et al. [38] which is given by

$$F^{\text{int}}_{\alpha\alpha}(r_{ij}) = \begin{cases} -S_{\alpha\alpha}\cos\left(\frac{3\pi}{4}q\right) & q \leq 2 \\ 0 & q > 2, \end{cases} \tag{6.1}$$

where $q = \frac{|r_{ij}|}{h}$ and $S_{\alpha\alpha}$ is the interaction strength of the PIF[2]. These pairwise forces are specifically designed to simulate the surface tension and are found to be in agreement with (4.35) [38, 29]. With the chosen pressure discretization and the EOS, we have that the surface tension due to F^p (expression (4.8)) is negligibly small compared to F^{int} and for ISPH simulations F^p is zero [38]. Substituting (6.1) and (4.7) into (4.35) yields

$$\sigma_{PIF} \approx \frac{2S_{\alpha\alpha}}{81}\frac{n^2 q_{cut}^4}{\pi^4}\left[9\pi^3 - 24\pi - 16\right], \tag{6.2}$$

and

$$p_v \approx -\frac{S_{\alpha\alpha}}{27}\frac{n^2 q_{cut}^3}{\pi^2}\left[9\pi^2 - 8\right], \tag{6.3}$$

where σ_{PIF} and p_v are the PIF induced surface tension and virial pressure. We consider an initial circular free surface droplet and verify the correctness of the above expressions according to Young-Laplace law. Based on Young-Laplace the measured pressure inside the droplet should equal

$$p_d \approx \frac{\sigma_{PIF}}{R} - p_v, \tag{6.4}$$

where R is the radius of the droplet. To avoid unknown consequences of the needed correction terms and prescribing a pressure value for ISPH[3], we will perform the free surface simulations with WCSPH. The initial radius of the droplet is set to $R = 0.125\ m$, the density to $\rho = 1\ \frac{kg}{m^3}$, the number density to $n = 25600$ and the viscosity to $\mu = 0.1\ Pas$. For the cut-off radius, we use the following set $q_{cut} = \{6L_0, 7L_0, 8L_0\}$ and lastly $S_{\alpha\alpha}$ is set to 0.01. The estimated and measured pressures are given in Table 6.2 and the pressure profile at $t = 1\ s$ is shown in Figure 6.6 a. From Figure 6.6 a, we observe pressure fluctuations near the free surface. For the mean pressure calculation we only consider particles away from the free surface, i.e. the normalized distance from the center should be smaller than 0.5. Furthermore, the fluctuating region increases for an increasing q_{cut}. This is expected, because for a greater compact radius, a particle i will interact with more surrounding particles and hence will sooner be affected by the free surface. Just like in Tartakovsky et al. [38] the SPH pressure is within 5% of the predicted values by (6.4). Lastly, because we use a basic WCSPH solver with no corrections, we observe a somewhat large spread in pressure values.

[2] We assumed that the pairwise forces have the same compact support as the kernel. Note that due to the Wendland kernel we have the relation $q_{cut} = 2h$, which explains $q < 2$.

[3] Remember that the PPE needs an additional BC condition in the form of a prescribed pressure, see subsection 3.4.

q_{cut}	$-p_v$	$\frac{\sigma_{PIF}}{R}$	p_d	Measured p_d	relative error
6	104.82	4.96	109.78	1.10×10^2	0.0020
7	166.46	9.19	175.65	1.76×10^2	0.0020
8	248.48	15.58	264.06	2.68×10^2	0.015

Table 6.2: The calculated values for the virial and measured pressure with a varying q_{cut}.

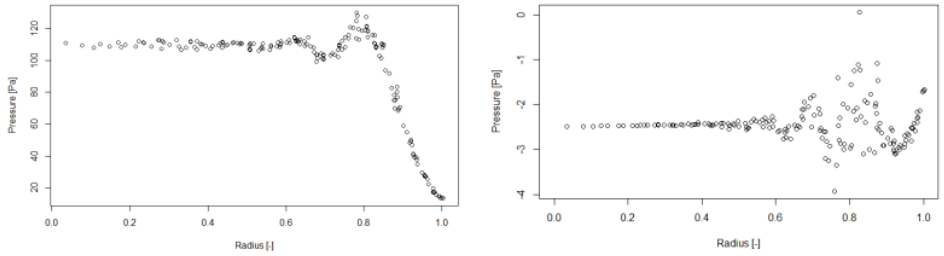

(a) (b)

Figure 6.6: Pressure profile of the inside droplet at time $t = 0.5\ s$ with Tartakovsky PIF ($F^{int}_{\alpha\alpha}$) (a) and the pressure profile for rheology PIF (F^{int}_{ij}) (b).

Next, we will investigate if (4.35) is still valid for the rheology pairwise forces given by [4]

$$F^{int}_{ij} = \begin{cases} m_j \frac{S_{ij}}{w}\left(-(r_{ij}-k)^2 + w\right),\ k = \frac{x_1^2 - x_2^2}{2x_1 - 2x_2},\ w = (x_2 - k)^2, & r_{ij} \le x_2 = q_{cut} \\ 0, & r_{ij} > x_2 = q_{cut}. \end{cases} \tag{6.5}$$

The surface tension and virial pressure due to the rheology pairwise forces are[5]

$$\sigma_{PIF} \approx -0.000261 n^2 m S_{ij} q^4_{cut}, \tag{6.6}$$

and

$$p_v \approx 0.317 n^2 m S_{ij} q^3_{cut}. \tag{6.7}$$

We observe a positive virial pressure and a negative surface tension. This means that our interaction force, for positive S_{ij}, will have a reducing affect on the surface tension. We will now perform the same simulations as for the Tartakovsky pairwise forces. However, since we consider the actual PIF of interest, we will perform more simulations and also vary the interaction strength. The results are shown in Table 6.3 and the pressure profile is shown in Figure 6.6 b. We again observe a 5% maximum difference between the measured and predicted pressures. However, due to the negative surface tension, the droplet cannot maintain the circular state and will deform in time. Furthermore, the simulation becomes unstable. In Tartakovsky and Panchenko [39] it was found that in order to ensure a stable simulation the virial pressure should be negative [6]. The pressure calculations are performed before the circular state is broken. However, the effect of the negative surface tension and positive virial pressure can still be observed in the pressure profile shown in Figure 6.6 b

[4] Important to note is that we have multiplied with the mass of particle m_j. Originally the pairwise rheology forces were introduced as an acceleration. Hence to abide by the estimate we needed to convert the acceleration to a force.

[5] In the SPH simulations the mass is kept constant, that is $m_j = m_i$.

[6] A possible explanation for this is that a negative virial prevents, to a certain extend, negative pressure values from occurring.

q_{cut}	S_{ij}	$-p_v$	$\frac{\sigma_{PIF}}{R}$	p_d	Measured p_d	$relative\ error$
4	10	-1.27	-2.1e-4	-1.27	-1.22	0.041
5	10	-2.48	-5.1e-4	-2.48	-2.46	0.008
6	10	-4.28	-1.1e-3	-4.28	-4.10	0.042
7	10	-6.8	-2.0e-3	-6.8	-6.48	0.047
4	5	-0.63	-1.0e-4	-0.63	-0.61	0.032
5	5	-1.24	-2.5e-4	-1.24	-1.23	0.008
6	5	-2.14	-5.3e-4	-2.14	-2.04	0.047
7	5	-3.40	-1.0e-3	-3.40	-3.23	0.050

Table 6.3: The calculated values for the virial and the measured pressure with varying q_{cut} and S_{ij}

In section 6.1, we saw that free surface simulations involving CSF suffers from instabilities. A way to solve this is to introduce an outer fluid, which will act as a stabilizer. To be able to combine CSF and PIF we have to verify if expressions (6.5) and (6.6) are applicable in the case that PIF will only be applied to the inner fluid (droplet). For multi-phase simulations, it is important to note that the initial form is not stable and that the droplet will expand over time. When an outer fluid is introduced, we have to be careful that the expansion does not result in a mixed layer. For WCSPH, the artificial speed of sound limits the threshold of compressibility to usually 1%. However, for ISPH the compressibilitity over time is unbounded [35]. To prevent mixing, we will perform simulations involving low values for S_{ij}. Furthermore, we start with an initial grid where a slight gap between the outer and inner fluid is introduced, see Figure 6.7 (a). We will perform both ISPH and WCSPH simulations. For WCSPH, we use periodic boundaries, but for ISPH we apply free-slip zero Dirichlet wall boundary conditions, see section 3.4. The pressure profiles are given in Figure 6.8. In accordance with the estimate, we observe a negative pressure inside the droplet. Even with the taken precautions, we could not prevent phase mixing and the simulations display instabilities over time, see Figure 6.7 (b). Plausible explanations are the negative surface tension and negative virial pressure. The negative pressures will attract the outer particles and the negative surface tension will deform the droplet. By changing the ratio of x_1 and x_2 in (6.5) we can enforce a positive surface tension. We change x_1 from $x_1 = 0.6671x_2$ to $x_1 = 0.5x_2$ which results in the following estimates

$$\sigma_{PIF} \approx 0.0444 n^2 m S_{ij} q_{cut}^4, \tag{6.8}$$

and

$$p_v \approx -0.209 n^2 m S_{ij} q_{cut}^3. \tag{6.9}$$

Figure 6.9 shows the pressure profiles for the new x_1 value. We first remark that during the simulation no mixing occurred and the initial circular form is preserved. Furthermore, we observe in Figure 6.9 that the ISPH pressure profile has a lower standard deviation than the WCSPH. This is likely related to the fact that we are using one of the most basic versions of WCSPH[7], which makes a comparison between WCSPH and ISPH unfair. For the ISPH pressure profiles we notice that for particles close to the wall, the influence of the prescribed zero pressure condition. That is, we observe a somewhat larger spread in pressure values. The spread occurs due to that for, particles with the same distance from the droplet center, some are affected by the wall boundary conditions, while others are not. The pressure differences for ISPH and WCPSH are $1.67\ Pa$ and $1.85\ Pa$, with a predicted difference of $1.75\ Pa$[8]. What is interesting in Figure 6.9 is the difference in pressure in the outer fluid. For ISPH, we enforce a zero pressure condition at the wall boundaries, resulting in an outer mean pressure of almost zero, namely $0.04\ Pa$. However, for WCSPH the mean value is $-0.27\ Pa$. A possible reason is that the size of the outer fluid is not sufficiently large. The particles at the periodic boundaries are still affected by the inner fluid. Therefore, the estimated pressure by (6.3) is divided between the inner en outer fluid.

[7] The code we are working with is specially designed for ISPH and only a basic version of WCSPH is implemented.
[8] Important to note is that the initial radius is $0.19\ m$ instead of $0.15\ m$.

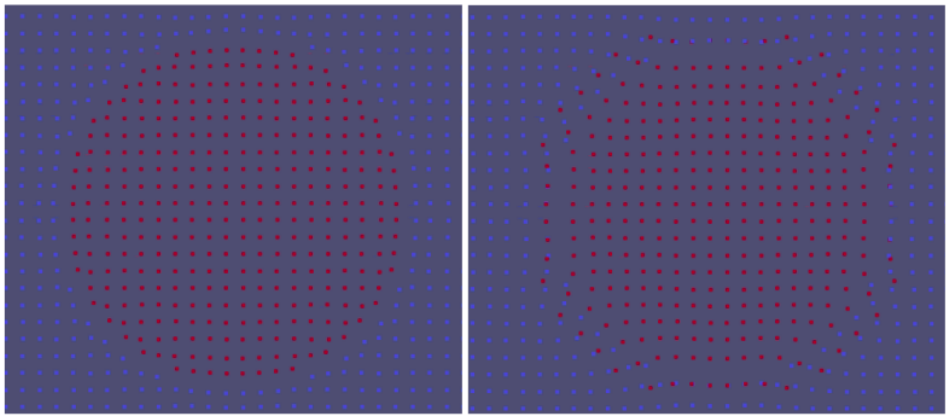

(a) (b)

Figure 6.7: Visualisation of the initial grid with the gap (a) and visualisation of the mixed layer, the instability and the deformation from the initial circular form.

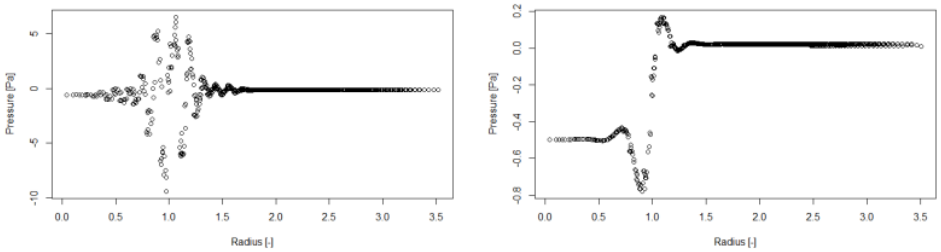

(a) (b)

Figure 6.8: Pressure for a two fluid simulation with rheology PIF (WCSPH) (a) and the pressure profile for ISPH (b). We used the following parameters: $S_{ij} = 1$ and $q_{cut} = 5L_0$.

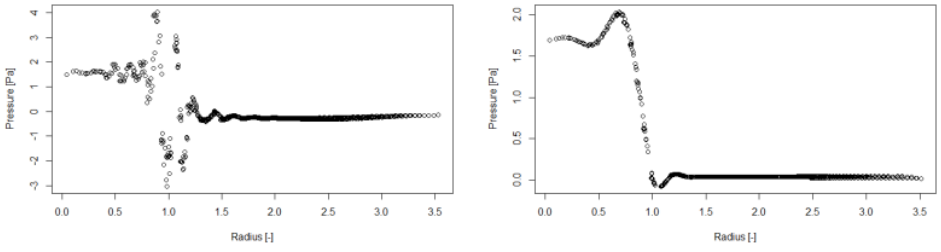

(a) (b)

Figure 6.9: Pressure for a two fluid simulation with rheology PIF (WCSPH) (a) and the pressure profile for ISPH (b). We used the following parameters: $q_{cut} = 5L_0$ and $S_{ij} = 5$.

By performing a long-time simulation with an ISPH solver, we observe an increasing gap between the fluids, which eventually leads to the termination of the simulation, see Figure 6.10 (a). The gap

seems to arise because the outer fluid is being compressed. The gap did not occur, when a WCSPH solver was used. However, by decreasing the artificial speed of sound, which allows for larger density fluctuations, we also detect the gap. A possible explanation for this might be that the compressibility in WCSPH is limited by the artificial speed of sound, which prevents the fluids from compressing. For ISPH, this is not the case, instead the density error can accumulate over time [35]. In Appendix A, we verify the accumulation of the density errors. We propose two solutions for the ISPH solver. The first solution involves a variant of the ISPH solver, namely the ISPH solver from Hu and Adams [15]. Instead of only using the DV condition, an intermediate time-step is introduced which is used to enforce the DI constrain described in section 3.2.1, resulting in a threshold on the density fluctuations. The second solution is using the particle shifting method explained in section 3.7.1. In this study, we choose the latter, which results in a stable simulation over time, with a final particle distribution as shown in Figure 6.10 (b).

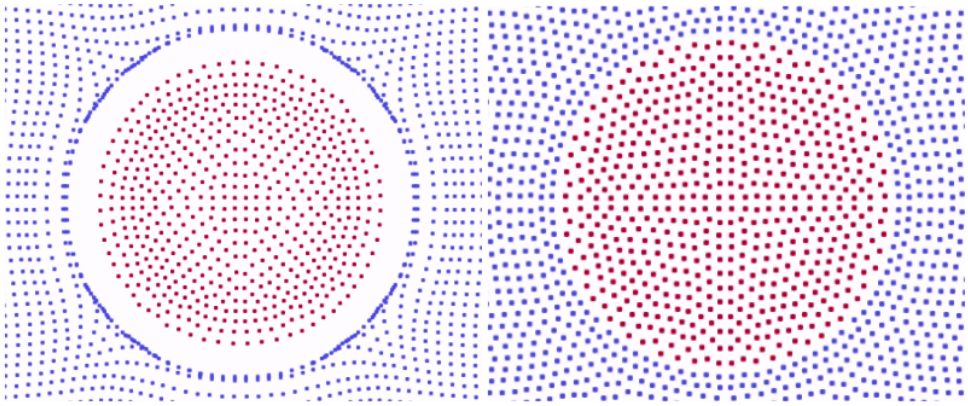

Figure 6.10: Visualization of the gap between the inner and outer fluid (a) and the particle distribution at the final time, when particle shifting is applied (b).

6.3.2. Oscillating droplet: analytical estimation

We will repeat the droplet oscillations, but now with the PIF. We will choose the value of S_{ij} in such a way that it corresponds to the surface tension values used in Figure 6.5 (b). The computational details are presented in Table 6.4. Important to note, is that instead of an initial divergence-free velocity field, we start with an ellipse. The reason for this is that the PIF increases the viscosity, which dampens the initial amplitude.

Parameter		Value
initial particle distance	L_0	$\frac{1}{60}m$
initial fluid density (droplet)	ρ_d	$1\frac{kg}{m^3}$
initial fluid density (outer)	ρ_l	$0.001\frac{kg}{m^3}$
dynamic viscosity (droplet)	μ_d	$0.05\frac{kg}{sm}$
dynamic viscosity (outer)	μ_d	$0.0005\frac{kg}{sm}$
initial radius	R	$0.163\ m$
number of particles	N	60×60
Major axis length	$-$	$24L_0$
Minor axis length	$-$	$16L_0$

Table 6.4: Computational details for the free droplet oscillations, where PIF are used instead of the CSF method.

The first simulation was performed with a cut-off radius q_{cut} of $6L_0$. However, we observed that the droplet did not attain the expected circular equilibrium form. Furthermore, the droplet reached an equilibrium state within the first oscillation. When increasing q_{cut}, the droplet did perform as expected.

e dependence on q_{cut} is also observed in Nair and Pöschel [29]. They argue that for smaller q_{cut}, the particles tend to "crystalize" to lower energy configurations, which leads to the observed overdamping [29]. We will therefore perform the simulations with a higher cut-off radius, namely $q_{cut} = 7.5L_0$. The droplet oscillations for S_{ij} values corresponding to a surface tension of $0.6, 0.8$ and $1.0\ N/m$ are shown in Figure 6.11. Additionally, the estimated and measured period are given in Table 6.5. It can be seen from the data in Table that there is a substantial difference between the measured and estimated surface tension. This may be explained by that the surface tension is not dominating the viscosity, which is required for (5.5) to be applicable. The used PIF is designed to simulate the fluid rheology and not the surface tension. Unfortunately, it is yet unknown what the contribution of the PIF is to the viscosity and elasticity of the fluid. To be able to predict the oscillations of a viscoelastic droplet we need to have a constitutive equation. However, the constitutive equation describing the PIF rheology is also unknown. Important to note is that for PIF designed specifically to simulate the surface tension the above method is valid [29]. We argue that their PIF induced viscosity and elasticity is much smaller, resulting in the required dominating surface tension.

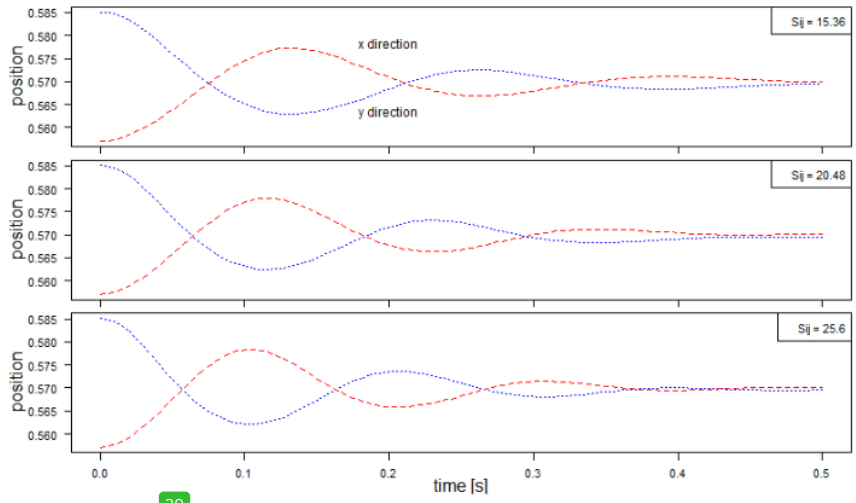

Figure 6.11: The position of the center of mass of the droplet shown over time. The corresponding surface tension values are $0.6, 0.8$ and $1.0\ N/m$

S_{ij}	Estimated σ_{PIF}	Period	Measured period	relative error	Measured σ_{PIF}
15.36	0.6	0.219	0.259	0.183	0.428
20.49	0.8	0.190	0.231	0.216	0.535
25.66	1.0	0.169	0.210	0.242	0.647

Table 6.5: The calculated values for the measured and estimate Period. Additionally, based on the measured period, we determine the corresponding "measured" surface tension.

6.4. Pairwise interactions combined with continuum surface force

We have verified the implementation of the CSF and the PIF methods. For the separate case, we were able to predict the surface tension accurately in a static test. For the dynamic surface tension, we found that the PIF induced surface tension is being underestimated. To our knowledge, there has been no cases where CSF and PIF are combined. In this section, we will repeat the previous experiments, but now with CSF and PIF combined. We start with the square deformation benchmark test. Furthermore, in the previous section, we observed that the pressure profile with a WCSPH solver contains larger fluctuations. Therefore, we will only perform simulations with an ISPH solver. We will first perform a small scale simulation, in order to investigate if CSF and PIF can be combined. The simulation is per-

formed with the corrections methods described in section 3.7. Additionally, we use periodic boundaries. Important here to note is that from here on out, we do not prescribe a pressure value, but instead make use of the built-in flag called “ksp constant null space” from the PETSc library. Figure 6.12 shows the droplet at different time instances and we observe that the simulation reaches an equilibrium.

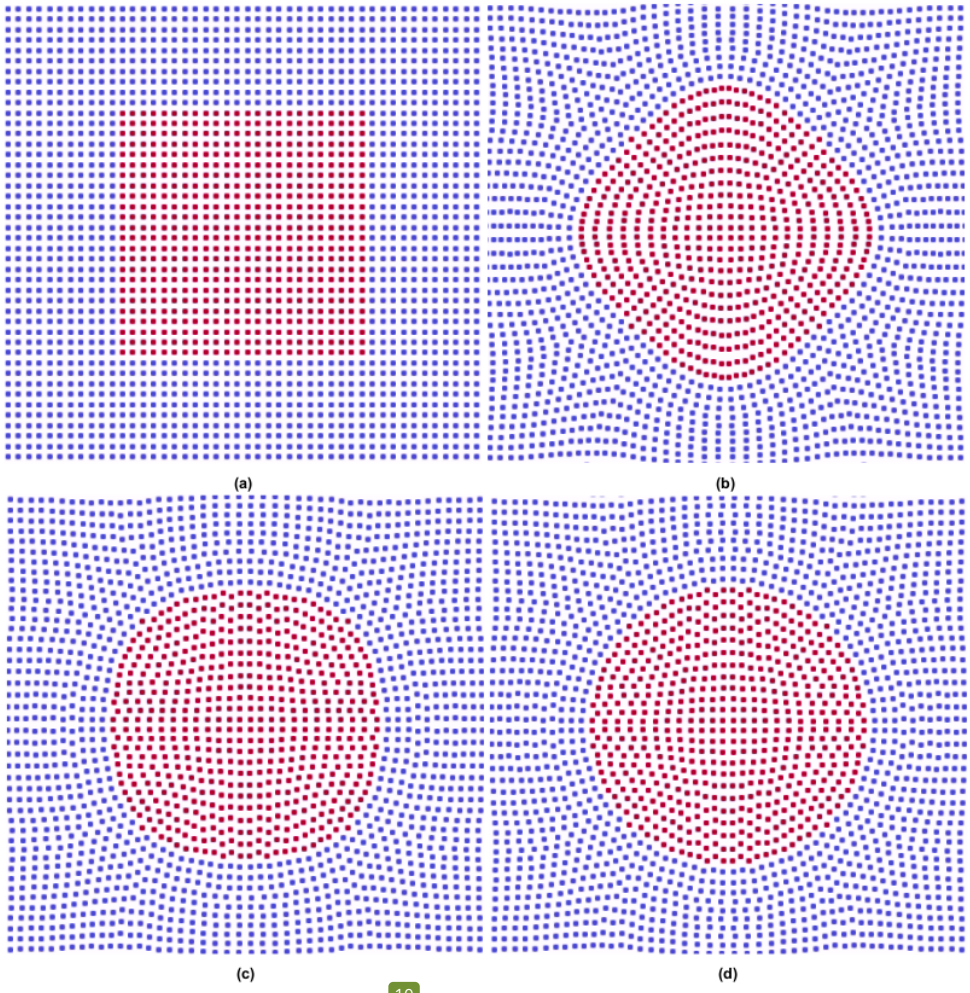

Figure 6.12: Droplet deformation at different time instances, namely t=0.0, 0.1, 0,3 and 0.5 s.

By assuming that we can just add the pressure contribution from CSF to the PIF pressure, we can express the droplet pressure in the following way

$$p_d \approx \frac{\sigma_{CSF}}{R} + \frac{\sigma_{PIF}}{R} - p_v. \tag{6.10}$$

To verify if (6.10) holds, we simulate the square droplet deformation with different CSF and PIF coefficients. The simulation parameters are given in Table 6.6. Furthermore, the individual contribution of the virial pressure and the PIF surface tension are given in Table 6.7. From Table 6.7, we observe that the main contribution to the pressure is due to the virial pressure. Figure 6.13 shows the pressure difference versus the CSF surface tension with different PIF coefficients and Figure 6.14 displays a zoomed in version to the more realistic surface tension values. Furthermore, Figure 6.15 shows the pressure

profile for a single simulation. From Figure 6.13, we note that the pressure estimated by (6.10) is in good agreement with the measured pressure differences, see also Appendix B for the relative error table [9]. This is a remarkable outcome since this speaks in favour of that the CSF and PIF contributions are decoupled forces. A note of caution is due here since the main contribution is due to the virial pressure. However, since the virial pressure works under the same principle as the PIF surface tension, it is likely that the PIF surface tension follows the same trend as the virial pressure. Another important remark is that the cut-off length plays an important role in the final equilibrium state. When the cut-off length is too small, the droplet does not attain a circular state. This is likely due to the same reason as for the PIF oscillating droplet test.

Parameter		Value
initial particle distance	L_0	$\frac{0.0018}{144} m$
cutoff radius	q_{cut}	$6.0L_0$
initial fluid density (droplet)	ρ_d	$1000\frac{kg}{m^3}$
initial fluid density (outer)	ρ_l	$1000\frac{kg}{m^3}$
dynamic viscosity (droplet)	μ_d	$0.05\frac{kg}{sm}$
dynamic viscosity (outer)	μ_d	$0.05\frac{kg}{sm}$
initial size (droplet)	$L_{x,d} \times L_{y,d}$	$16L_0 \times 16L_0$
number of particles	N	144×144

Table 6.6: Computational details for the square deformation droplet test, where PIF and the CSF method are simultaneously used.

S_{ij}	p_v	$\frac{\sigma_{PIF}}{R}$	p_{PIF}
1000	-5.65$\times 10^2$	4.50$\times 10^1$	6.10$\times 10^2$
10000	-5.65$\times 10^3$	4.50$\times 10^2$	6.10$\times 10^3$

Table 6.7: The calculated values for the virial pressure and surface tension due to PIF, where p_{PIF} is the pressure due to the PIF induced surface tension minus the virial pressure.

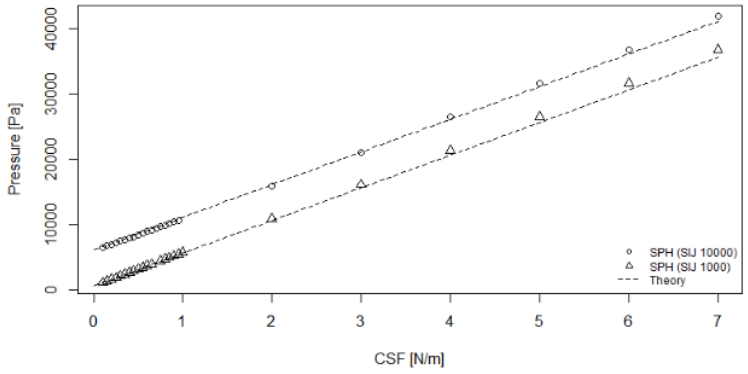

Figure 6.13: The pressure difference versus the CSF surface tension with two different interaction strengths. The dashed line is the total predicted pressure difference due to CSF and PIF.

[9] The maximum relative error is 0.0224.

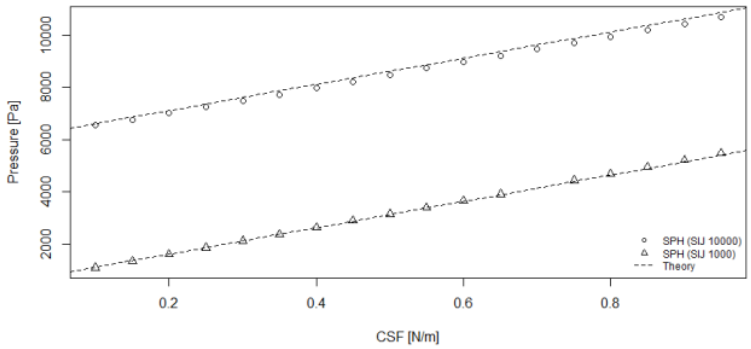

Figure 6.14: The pressure difference versus the CSF surface tension with two different interaction strengths. However, now the relevant surface tension values are shown. The dashed line is the total predicted pressure difference due to CSF and PIF.

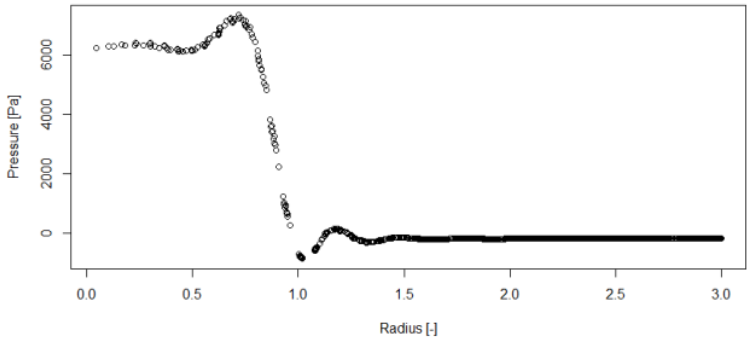

Figure 6.15: Pressure profile for $\sigma_{CSF} = 0.1\ N/m$ and $S_{ij} = 1000\ m/s^2$. For visual purposes we only took particles with a certain distance from the center, namely three times the radius.

We will now investigate if the same decoupled relation holds, when considering an oscillating droplet. However, since, most likely, we are not in a surface tension dominating regime, we will also use the measured surface tension values from Table 6.5. We use the same numerical parameters as given in Table 6.4. Figure 6.16 shows the measured period versus the CSF surface tension combined with different interaction strengths. From Figure 6.16, we observe that the period is best predicted by the CSF surface tension plus the measured σ_{PIF} (green dashed line). Furthermore, Figure 6.16 appears to support the assumption that the CSF and PIF surface tensions can be seen as decoupled forces. However, in order to substantiate the claim, we go to a higher resolution. That is, we increase the total number of particles from 60×60 to 72×72, increase the initial radius from $0.1633\ m$ to 0.248452 m and increase the cut-off radius from $7.5L_0$ to $8L_0$. We set S_{ij} equal to $17.086\ m/s^2$, corresponding to an estimated surface tension of $0.6\ N/m$. Figure 6.17 shows the higher resolution results. We observe in Figure 6.17, contrary to the previous results, that the measured periods are now in between the theoretical periods. This is also what we expected in the previous results, since the additional CSF should increase the dominance of the surface tension. Therefore, inclining to the theoretical period based on the estimated surface tension. A possible explanation why this did not occur for the lower resolution simulations is that the accuracy is not sufficient. To be more specific, too few particles were

used to create the inner droplet. However, to be able to make hard claims about the relation between CSF and PIF further research should be performed. An important remark is that we do not know how the PIF induced viscosity and elasticity scales with the compact radius q_{cut}. For σ_{PIF} we know that it is proportional to q_{cut}^4. When the rheology does not follow the same scaling, it will cause problems when changing q_{cut} which is needed to increase the resolution.

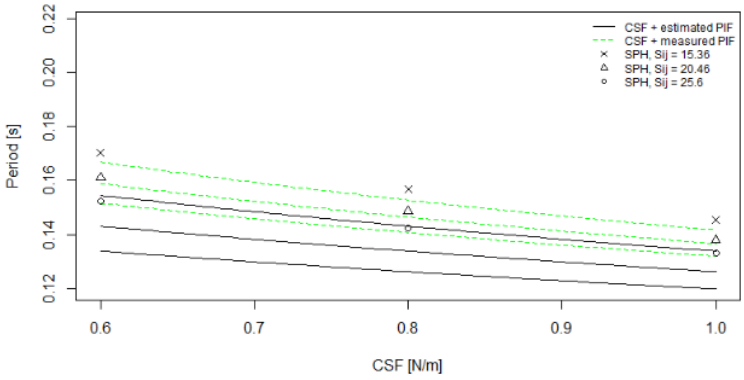

Figure 6.16: The period due to the combined CSF and PIF surface tension. The green dashed line represent the theoretical period based on the CSF and the measured PIF surface tension. The solid line uses the predicted PIF surface tension values. These values are 0.6, 0.8 and 1.0 N/m corresponding to S_{ij} = 15.36, 20.46 and 25.6 m/s^2.

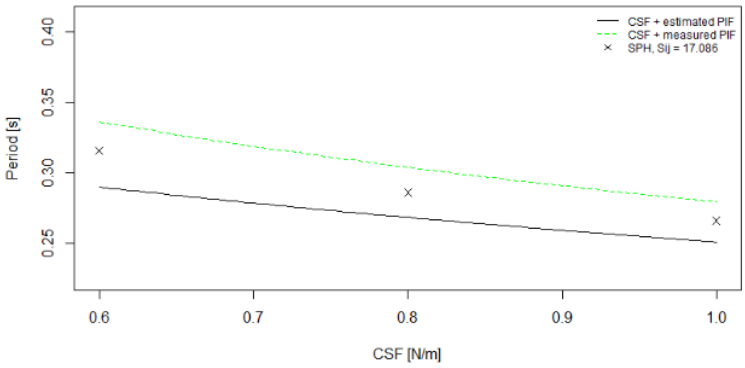

Figure 6.17: The period due to the combined CSF and PIF surface tension. The green dashed line represent the theoretical period based on the CSF and the measured PIF surface tension. The solid line uses the predicted PIF surface tension values.

Up to this point, we used CSF to increase the PIF induced surface tension. We will now investigate if we can reduce the surface tension, by using a negative CSF coefficient. We start with the static test. The computational details are 139n in Table 6.8. We choose the interaction strength such that it corresponds to a surface tension of 1.0 N/m. The pressure contributions of the virial pressure and PIF surface tension are

$$p_v = -5.03 \times 10^5 Pa,$$

and

$$\frac{\sigma_{PIF}}{R} = 4.43 \times 10^4 Pa.$$

Figure 6.18 shows the measured pressures differences versus the negative CSF coefficients. From Figure 6.18 we observe that we can indeed lower the PIF induced surface tension. Noteworthy is that the droplet, for $\sigma_{CSF} = -1.0\ N/m$, reached a quasi circular form. In theory the surface tension should be equal to zero. However, a possible explanation for the quasi circular form is that the PIF induced surface tension works on the entire droplet surface, whereas CSF only acts in regions with high curvatures. For larger negative CSF coefficients, the droplet gets torn apart, resulting in the early termination of the simulation.

Parameter		Value
initial particle distance	L_0	$\frac{0.001}{80} m$
cutoff radius	q_{cut}	$7.5L_0$
initial fluid density (droplet)	ρ_d	$1000\frac{kg}{m^3}$
initial fluid density (outer)	ρ_l	$1000\frac{kg}{m^3}$
dynamic viscosity (droplet)	μ_d	$0.05\frac{kg}{sm}$
dynamic viscosity (outer)	μ_d	$0.05\frac{kg}{sm}$
initial size (droplet)	$L_{x,d} \times L_{y,d}$	$16L_0 \times 16L_0$
number of particles	N	80×80
PIF interaction strength	S_{ij}	$45511.11\frac{m}{s^2}$

Table 6.8: Computational details for the square deformation droplet, where PIF are combined with a negative CSF.

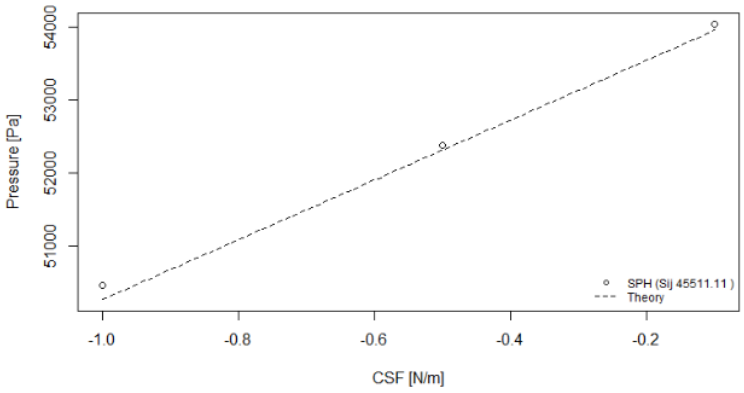

Figure 6.18: The pressure difference versus the negative CSF surface tension. The interaction strength corresponds to a surface tension of $1\ N/m$. The chosen CSF coefficient are -1.0, -0.5 and $-0.1\ N/m$.

We will now consider an oscillating droplet. We use the same parameters as given in Table 6.4. Additionally, we use a cut-off length q_{cut} of $8L_0$ and an interaction strength S_{ij} of 19.775 m/s^2, corresponding to an estimated surface tension of 1.0 N/m. Figure 6.19 presents the obtained periods. We first note that all periods are between the theoretical periods. Secondly, we observe an decreasing trend in the period length along the CSF coefficient. Unfortunately, substantial claims cannot be made based on Figure 6.19[10].

[10]We suggest repeating the same dynamic test, but now with the PIF from Tartakovsky and perform a convergence study.

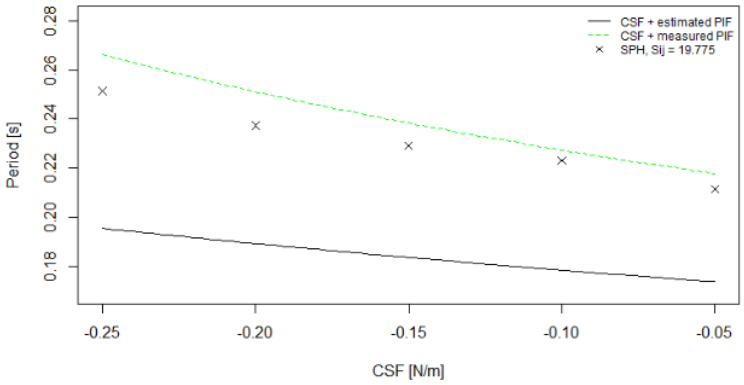

Figure 6.19: The period versus the combined negative CSF and PIF surface tension.The green dashed line represent the theoretical period based on the CSF and the measured PIF surface tension. The solid line uses the predicted PIF surface tension value. The interaction strength corresponds to an estimated surface tension of 1 N/m.

7

Conclusion and Recommendations

In this study, we quantify the effect of Particle Interaction Forces (PIF) on the surface tension and investigated the possibility to further calibrate the PIF induced surface tension to match the desired surface tension. To further calibrate the surface tension, we use the Continuum Surface Force (CSF) method.

In an earlier study, PIF were used to change the rheological fluid properties. However, it was found that PIF also influences the surface tension and introduces an additional pressure, namely the "virial" pressure. By following the derivation of Tartakovsky and Panchenko [39], we derived an expression to estimate the PIF induced surface tension and virial pressure. These estimates are validated in a static and dynamic setting. A limitation of this study is that we do not know what kind of rheological behaviour the PIF produces, which greatly limits the possible dynamic tests to measure the surface tension. The static test involves a circular droplet inside a second fluid, acting as a stabilizer. Based on Young-Laplace law we can determine the surface tension by measuring the pressure difference. The dynamic test simulates an oscillating droplet, where the surface tension can be determined by determining the oscillation period of the droplet. It is important to mention that the dynamic test is only valid when the surface tension is the dominating force.

We observed that to prevent instabilities from occurring, a positive virial pressure is needed. Furthermore, for both the static and dynamic tests a relatively large compact radius is required to prevent overdamping from happening and for the droplet to reach the circular form in equilibrium.

For the static test, we can predict the PIF induced surface tension and virial pressure. Furthermore, results suggest that when CSF and PIF are combined, the resulting total surface tension is just the sum of the separate values, i.e. CSF and PIF are decoupled forces. Important to note is that the virial pressure is one order of magnitude larger than the PIF surface tension pressure. However, its contribution is still significant. Another noteworthy finding is that correction methods, such as particle shifting or an improved version of ISPH, are needed when an ISPH solver is used. Most likely this is due to the fact that these corrections prevent large density fluctuations from occurring, which is in agreement with that for a WCSPH solver no corrections are needed. In WCSPH, the density fluctuations are limited by the artificial speed of sound, preventing the gap from occurring between different phases.

For the dynamic tests, we observed an underestimated surface tension due to the PIF. A plausible reason is that the PIF surface tension is not a dominant force over the viscoelastic properties which are also induced by PIF. Contrary to the static case, when we combine CSF and PIF, we cannot make substantial claims about the total surface tension.

Preliminary results show that we can also lower the PIF induced surface tension to a certain extent, with a negative CSF coefficient. A note of caution is at place here since due to limited time, not an extensive study was performed.

7.1. Recommendations for further research

This study shows promising results to enable us to further tune the PIF induced surface tension. However, further research is needed. We suggest the following recommendations

- A study to find the constitutive equation describing the PIF induced fluid rheology. With the constitutive equation, we can then investigate the CSF and PIF relation in a non-dominating surface tension regime.
- Research to determine to what extent we can lower the PIF induced surface tension with CSF. Additionally, performing a stability analysis in case a negative surface tension coefficient is used.
- Investigating if the found relations for the combination of CSF and PIF are still valid for a free surface droplet.
- Performing a convergence study, in the case that CSF and PIF are combined. Additionally, quantifying the minimum needed compact radius, in different resolutions, for the PIF method.

References

[1] S Adami and J Account. “Comparison of interface models to account for surface tension in SPH method”. In: (2020), pp. 714–725.

[2] S. Adami, X. Y. Hu, and N. A. Adams. “A new surface-tension formulation for multi-phase SPH using a reproducing divergence approximation”. In: *Journal of Computational Physics* 229.13 (2010), pp. 5011–5021. ISSN: 10902716. DOI: 10.1016/j.jcp.2010.03.022.

[3] Nadir Akinci, Gizem Akinci, and Matthias Teschner. “Versatile surface tension and adhesion for SPH fluids”. In: *ACM Transactions on Graphics* 32.6 (2013). ISSN: 07300301. DOI: 10.1145/2508363.2508395.

[4] Arne Bøckmann, Olga Shipilova, and Geir Skeie. “Incompressible SPH for free surface flows”. In: *Computers and Fluids* 67 (2012), pp. 138–151. ISSN: 00457930. DOI: 10.1016/j.compfluid.2012.07.007.

[5] J. Bonet and T. S.L. Lok. “Variational and momentum preservation aspects of Smooth Particle Hydrodynamic formulations”. In: *Computer Methods in Applied Mechanics and Engineering* 180.1-2 (1999), pp. 97–115. ISSN: 00457825. DOI: 10.1016/S0045-7825(99)00051-1.

[6] Alex D Chow et al. “Incompressible SPH (ISPH) with fast Poisson solver on a GPU”. In: *Computer Physics Communications* 226 (2018), pp. 81–103. ISSN: 0010-4655. DOI: 10.1016/j.cpc.2018.01.005.

[7] Paul W. Cleary and Joseph J. Monaghan. “Conduction Modelling Using Smoothed Particle Hydrodynamics”. In: *Journal of Computational Physics* 148.1 (1999), pp. 227–264. ISSN: 00219991. DOI: 10.1006/jcph.1998.6118.

[8] Walter Dehnen and Hossam Aly. “Improving convergence in smoothed particle hydrodynamics simulations without pairing instability”. In: *Monthly Notices of the Royal Astronomical Society* 425.2 (2012), pp. 1068–1082. ISSN: 00358711. DOI: 10.1111/j.1365-2966.2012.21439.x.

[9] Leonardo Di G. Sigalotti et al. “On the kernel and particle consistency in smoothed particle hydrodynamics”. In: *Applied Numerical Mathematics* 108 (2016), pp. 242–255. ISSN: 0168-9274. DOI: https://doi.org/10.1016/j.apnum.2016.05.007.

[10] Jan Philipp Fürstenau, Christian Weißenfels, and Peter Wriggers. “Free surface tension in incompressible smoothed particle hydrodynamcis (ISPH)”. In: *Computational Mechanics* 65.2 (2020), pp. 487–502. ISSN: 14320924. DOI: 10.1007/s00466-019-01780-6.

[11] A Halik et al. “Numerical Modeling for Discrete Multibody Interaction and Multifeild Coupling Dynamics Using the SPH Method”. Dutch. In: *Mathematical Problems in Engineering* 2015 (2015), pp. 1–12. DOI: 10.1155/2015/205976.

[12] Xiaowei He et al. “Robust Simulation of Small-Scale Thin Features in SPH-based Free Surface Flows”. In: *Life.Kunzhou Net* 1.212 (2014), pp. 1–8. ISSN: 07300301.

[13] Manuel Hirschler et al. “Modeling of droplet collisions using Smoothed Particle Hydrodynamics”. In: *International Journal of Multiphase Flow* 95 (2017), pp. 175–187. ISSN: 03019322. DOI: 10.1016/j.ijmultiphaseflow.2017.06.002.

[14] Manuel Hirschler et al. “Open boundary conditions for ISPH and their application to micro-flow”. In: *Journal of Computational Physics* 307 (2016), pp. 614–633. ISSN: 10902716. DOI: 10.1016/j.jcp.2015.12.024.

[15] X. Y. Hu and N. A. Adams. “An incompressible multi-phase SPH method”. In: *Journal of Computational Physics* 227.1 (2007), pp. 264–278. ISSN: 10902716. DOI: 10.1016/j.jcp.2007.07.013.

[16] Markus Huber et al. “Evaluation of Surface Tension Models for SPH-Based Fluid Animations Using a Benchmark Test”. In: *VRIPHYS* (2015).

[17] Malvern Instruments. “A basic introduction to rheology”. In: *Malvern Instruments Limited* (2016).

[18] Yongsong Jiang et al. “A second-order numerical method for elliptic equations with singular sources using a local filter”. In: *Chinese Journal of Aeronautics* 26.6 (2013), pp. 1398–1408. ISSN: 10009361. DOI: 10.1016/j.cja.2013.07.004.

[19] Franz Keller. *Simulation of the Morphogenesis of Open – porous Materials*. Logos Verlag, 2015, p. 335. ISBN: ISBN 978-3-8325-3962-7.

[20] P Kunz et al. “Study of Multi-phase Flow in Porous Media : Comparison of SPH Simulations with Micro-model Experiments”. In: *Transport in Porous Media* 114.2 (2016), pp. 581–600. ISSN: 1573-1634. DOI: 10.1007/s11242-015-0599-1.

[21] Yixin Lin, G R Liu, and Guangyu Wang. “A particle-based free surface detection method and its application to the surface tension effects simulation in smoothed particle hydrodynamics (SPH)”. In: *Journal of Computational Physics* 383 (2019), pp. 196–206. ISSN: 0021-9991. DOI: 10.1016/j.jcp.2018.12.036.

[22] M B Liu, G R Liu. *Smoothed Particle Hydrodynamics (SPH): an Overview and Recent Developments*. 2010, pp. 25–76. ISBN: 1183101090. DOI: 10.1007/s11831-010-9040-7.

[23] Antonin Marchand et al. “Why is surface tension a force parallel to the interface?” In: *American Journal of Physics* 79.10 (2011), pp. 999–1008. ISSN: 0002-9505. DOI: 10.1119/1.3619866. arXiv: 1211.3854.

[24] Tara McHugh. “The Significance of Spray-Drying”. In: *Food Technology* 72.4 (2018).

[25] J. J. Monaghan. “Smoothed particle hydrodynamics”. In: *Reports on Progress in Physics* 68.8 (2005), pp. 1703–1759. ISSN: 00344885. DOI: 10.1088/0034-4885/68/8/R01.

[26] Joseph P Morris. “Simulating surface tension with smoothed particle hydrodynamics”. In: *INTERNATIONAL JOURNAL FOR NUMERICAL METHODS IN FLUIDS Int. J. Numer. Meth. Fluids 2000; 33: 333–353 Simulating* 6 (2000), pp. 333–353.

[27] Joseph P. Morris, Patrick J. Fox, and Zhu Yi. “Modeling low Reynolds number incompressible flows with curved boundaries using SPH”. In: *International Journal for Numerical Methods in Fluids* 13 (1997), pp. 214–226. ISSN: 02712091. DOI: 10.1002/fld.2600.

[28] Faith A. Morrison. *Understanding Rheology*. Oxford University Press, 2001. ISBN: 978-0-19-514166-5.

[29] Prapanch Nair and Thorsten Pöschel. “Dynamic capillary phenomena using Incompressible SPH”. In: *Chemical Engineering Science* 176 (2018), pp. 192–204. ISSN: 00092509. DOI: 10.1016/j.ces.2017.10.042.

[30] J. J. Padding. “Particle-Based Simulations Lecture Notes”. In: (2017), pp. 109–132, 141–148.

[31] M S Shadloo, G Oger, and D Le Touzé. “Smoothed particle hydrodynamics method for fluid flows , towards industrial applications : Motivations , current state , and challenges”. In: 136 (2016), pp. 11–34. DOI: 10.1016/j.compfluid.2016.05.029.

[32] Meng Shuangshuang et al. “The study on performances of kernel types in solid dynamic problems by smoothed particle hydrodynamics”. In: *Computational Particle Mechanics* (2020). ISSN: 2196-4378. DOI: 10.1007/s40571-020-00339-0.

[33] Leonardo Di G. Sigalotti et al. “A new insight into the consistency of the SPH interpolation formula”. In: *Applied Mathematics and Computation* 356 (2019), pp. 50–73. ISSN: 0096-3003. DOI: https://doi.org/10.1016/j.amc.2019.03.018.

[34] Fedir V. Sirotkin and Jack J. Yoh. “A new particle method for simulating breakup of liquid jets”. In: *Journal of Computational Physics* 231.4 (2012), pp. 1650–1674. ISSN: 10902716. DOI: 10.1016/j.jcp.2011.10.020.

[35] K. Szewc, J. Pozorski, and J. P. Minier. “Analysis of the incompressibility constraint in the smoothed particle hydrodynamics method”. In: *International Journal for Numerical Methods in Engineering* 92.4 (2012), pp. 343–369. ISSN: 00295981. DOI: 10.1002/nme.4339.

[36] K. Szewc, J. Pozorski, and J. P. Minier. “Simulations of single bubbles rising through viscous liquids using Smoothed Particle Hydrodynamics”. In: *International Journal of Multiphase Flow* 50.October (2013), pp. 98–105. ISSN: 03019322. DOI: 10.1016/j.ijmultiphaseflow.2012.11.004.

[37] Kamil Szewc. “Development of Smoothed Particle Hydrodynamics approach for modelling of multiphase flows with Kamil Szewc ”. In: (2013).

[38] A. M. Tartakovsky et al. “Smoothed particle hydrodynamics and its applications for multiphase flow and reactive transport in porous media”. In: *Computational Geosciences* 20.4 (2016), pp. 807–824. ISSN: 15731499. DOI: 10.1007/s10596-015-9468-9.

[39] Alexandre M. Tartakovsky and Alexander Panchenko. “Pairwise Force Smoothed Particle Hydrodynamics model for multiphase flow: Surface tension and contact line dynamics”. In: *Journal of Computational Physics* 305 (2016), pp. 1119–1146. ISSN: 10902716. DOI: 10.1016/j.jcp.2015.08.037.

[40] Mark Van der Linde. “Viscoelasticity in SPH through particle interactions”. PhD thesis. TU Delft, 2020.

[41] Rui Xu, Peter Stansby, and Dominique Laurence. “Accuracy and stability in incompressible SPH (ISPH) based on the projection method and a new approach”. In: *Journal of Computational Physics* 228.18 (2009), pp. 6703–6725. ISSN: 10902716. DOI: 10.1016/j.jcp.2009.05.032.

[42] Wei Yu et al. “Theory for drop deformation in viscoelastic systems”. In: *Journal of Rheology* 48.2 (2004), pp. 417–438. ISSN: 0148-6055. DOI: 10.1122/1.1647559.

A

Relative error density

In contrary to what the name suggest the ISPH method does not result in a constant density. To estimate the density errors, we will determine two quantities: the mean density off the droplet $\overline{\rho}(t)$ and the root mean square of the density fluctuations $\rho_{rms}(t)$. To compute these quantities we use the same expressions as in Szewc, Pozorski, and Minier [35]. The mean density $\overline{\rho}(t)$ is given by

$$\overline{\rho}(t) = \frac{1}{N} \sum_i m_i \sum_j W_{ij}, \tag{A.1}$$

and the density fluctuation $\rho_{rms}(t)$ is given by

$$\rho_{rms}(t) = \sqrt{\frac{1}{N} \sum_i \left(m_i \sum_j W_{ij} - \overline{\rho}(t) \right)^2}. \tag{A.2}$$

Figure A.1 shows the density mean value and the r.m.s over time for a surface tension driven deformation. In Figure A.1, we observe for the ISPH simulation an accumulation of errors during the simulation, which is in agreement with the results from Szewc, Pozorski, and Minier [35]. Secondly, for the WCSPH solver we observe a stagnated mean density and a r.m.s. which remains less than 2% of the initial density.

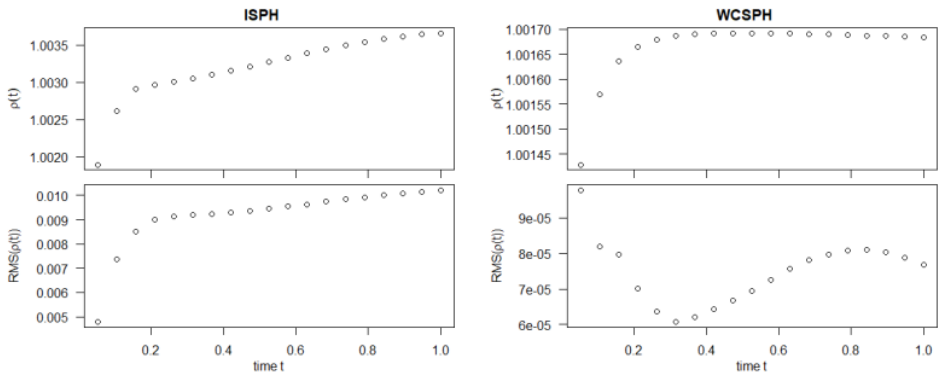

Figure A.1: The density mean value and the r.m.s obtained for a surface tension driven deformation.

B

Relative error pressure: CSF and PIF

We present in table B.1 the relative error due to the combined effect of CSF and PIF. Furthermore, we also present the separate contribution to the pressure, namely CSF and PIF.

S_{ij}	p_{PIF}	σ_{CSF}	p_{CSF}	Total pressure	Measured pressure	relative error
1000	6.10×10^{2}	0.1	5.00×10^{2}	1.10×10^{3}	1.09×10^{3}	0.0091
1000	6.10×10^{2}	0.15	7.50×10^{2}	1.36×10^{3}	1.34×10^{3}	0.012
1000	6.10×10^{2}	0.2	1.00×10^{3}	1.61×10^{3}	1.60×10^{3}	0.0063
1000	6.10×10^{2}	0.25	1.25×10^{3}	1.86×10^{3}	1.86×10^{3}	0.0
1000	6.10×10^{2}	0.3	1.50×10^{3}	2.11×10^{3}	2.12×10^{3}	0.0047
1000	6.10×10^{2}	0.35	1.75×10^{3}	2.36×10^{3}	2.38×10^{3}	0.0085
1000	6.10×10^{2}	0.4	2.00×10^{3}	2.61×10^{3}	2.63×10^{3}	0.0077
1000	6.10×10^{2}	0.45	2.25×10^{3}	2.86×10^{3}	2.90×10^{3}	0.014
1000	6.10×10^{2}	0.5	2.50×10^{3}	3.11×10^{3}	3.14×10^{3}	0.0097
1000	6.10×10^{2}	0.55	2.75×10^{3}	3.36×10^{3}	3.40×10^{3}	0.012
1000	6.10×10^{2}	0.6	3.00×10^{3}	3.61×10^{3}	3.66×10^{3}	0.0028
1000	6.10×10^{2}	0.65	3.25×10^{3}	3.86×10^{3}	3.91×10^{3}	0.013
-	-	0.7	-	-	-	
1000	6.10×10^{2}	0.75	3.75×10^{3}	4.36×10^{3}	4.44×10^{3}	0.018
1000	6.10×10^{2}	0.8	4.00×10^{3}	4.61×10^{3}	4.70×10^{3}	0.020
1000	6.10×10^{2}	0.85	4.25×10^{3}	4.86×10^{3}	4.95×10^{3}	0.019
1000	6.10×10^{2}	0.9	4.50×10^{3}	5.11×10^{3}	5.22×10^{3}	0.022
1000	6.10×10^{2}	0.95	4.75×10^{3}	5.36×10^{3}	5.48×10^{3}	0.022
1000	6.10×10^{2}	1.0	5.00×10^{3}	5.61×10^{3}	5.73×10^{3}	0.021
10000	6.10×10^{3}	0.1	5.00×10^{2}	6.60×10^{3}	6.54×10^{3}	0.0091
10000	6.10×10^{3}	0.15	7.50×10^{2}	6.85×10^{3}	6.77×10^{3}	0.012
10000	6.10×10^{3}	0.2	1.00×10^{3}	7.10×10^{3}	7.01×10^{3}	0.013
10000	6.10×10^{3}	0.25	1.25×10^{3}	7.35×10^{3}	7.25×10^{3}	0.014
10000	6.10×10^{3}	0.3	1.50×10^{3}	7.60×10^{3}	7.49×10^{3}	0.015
10000	6.10×10^{3}	0.35	1.75×10^{3}	7.85×10^{3}	7.73×10^{3}	0.015
10000	6.10×10^{3}	0.4	2.00×10^{3}	8.10×10^{3}	7.98×10^{3}	0.015
10000	6.10×10^{3}	0.45	2.25×10^{3}	8.350×10^{3}	8.22×10^{3}	0.016
10000	6.10×10^{3}	0.5	2.50×10^{3}	8.60×10^{3}	8.48×10^{3}	0.014
10000	6.10×10^{3}	0.55	2.75×10^{3}	8.85×10^{3}	8.73×10^{3}	0.014
10000	6.10×10^{3}	0.6	3.00×10^{3}	9.10×10^{3}	8.97×10^{3}	0.014
10000	6.10×10^{3}	0.65	3.25×10^{3}	9.35×10^{3}	9.22×10^{3}	0.014
10000	6.10×10^{3}	0.7	3.50×10^{3}	9.60×10^{3}	9.46×10^{3}	0.015
10000	6.10×10^{3}	0.75	3.75×10^{3}	9.85×10^{3}	9.71×10^{3}	0.014
10000	6.10×10^{3}	0.8	4.00×10^{3}	1.01×10^{4}	9.94×10^{3}	0.016
10000	6.10×10^{3}	0.85	4.25×10^{3}	1.04×10^{4}	1.02×10^{4}	0.019
10000	6.10×10^{3}	0.9	4.50×10^{3}	1.06×10^{4}	1.04×10^{4}	0.019
10000	6.10×10^{3}	0.95	4.75×10^{3}	1.09×10^{3}	1.07×10^{4}	0.018
-	-	1.0	-	-		

Table B.1: The relative error when CSF and PIF are combined.

Final_thesis_kjeld_broekema.pdf

ORIGINALITY REPORT

16%	11%	12%	4%
SIMILARITY INDEX	INTERNET SOURCES	PUBLICATIONS	STUDENT PAPERS

PRIMARY SOURCES

1	Alexandre M. Tartakovsky, Alexander Panchenko. "Pairwise Force Smoothed Particle Hydrodynamics model for multiphase flow: Surface tension and contact line dynamics", Journal of Computational Physics, 2016 Publication	1%
2	pastel.archives-ouvertes.fr Internet Source	1%
3	hdl.handle.net Internet Source	1%
4	Manuel Hirschler, Philip Kunz, Manuel Huber, Friedemann Hahn, Ulrich Nieken. "Open boundary conditions for ISPH and their application to micro-flow", Journal of Computational Physics, 2016 Publication	<1%
5	hal-emse.ccsd.cnrs.fr Internet Source	<1%
6	arxiv.org Internet Source	<1%

7	Submitted to Technische Universiteit Delft Student Paper	<1 %
8	Manuel Hirschler, Guillaume Oger, Ulrich Nieken, David Le Touzé. "Modeling of droplet collisions using Smoothed Particle Hydrodynamics", International Journal of Multiphase Flow, 2017 Publication	<1 %
9	hal.archives-ouvertes.fr Internet Source	<1 %
10	www.tandfonline.com Internet Source	<1 %
11	Joseph P. Morris. "Simulating surface tension with smoothed particle hydrodynamics", International Journal for Numerical Methods in Fluids, 2000 Publication	<1 %
12	M. B. Liu. "Smoothed Particle Hydrodynamics (SPH): an Overview and Recent Developments", Archives of Computational Methods in Engineering, 02/13/2010 Publication	<1 %
13	Ronney Rodrigues Agra. "Influência da temperatura no comportamento do concreto com diferentes teores de fibras de aço.", Universidade de Sao Paulo, Agencia USP de	<1 %

	Gestao da Informacao Academica (AGUIA), 2020 Publication	
14	d-nb.info Internet Source	<1 %
15	dokumen.pub Internet Source	<1 %
16	kanazawa-u.repo.nii.ac.jp Internet Source	<1 %
17	Manuel Hopp-Hirschler, Mostafa Safdari Shadloo, Ulrich Nieken. "A Smoothed Particle Hydrodynamics Approach for Thermo-Capillary Flows", Computers & Fluids, 2018 Publication	<1 %
18	Submitted to Heriot-Watt University Student Paper	<1 %
19	orca.cf.ac.uk Internet Source	<1 %
20	Submitted to Cranfield University Student Paper	<1 %
21	mafiadoc.com Internet Source	<1 %
22	onlinelibrary.wiley.com Internet Source	<1 %
23	aapt.scitation.org Internet Source	

		<1%
24	open.library.ubc.ca Internet Source	<1%
25	Leonardo Di G. Sigalotti, Otto Rendón, Jaime Klapp, Carlos A. Vargas, Fidel Cruz. "A new insight into the consistency of the SPH interpolation formula", Applied Mathematics and Computation, 2019 Publication	<1%
26	amiemt-journal.com Internet Source	<1%
27	Submitted to University of Nottingham Student Paper	<1%
28	spectrum.library.concordia.ca Internet Source	<1%
29	Massoud Rezavand, Mohammad Taeibi-Rahni, Wolfgang Rauch. "An ISPH scheme for numerical simulation of multiphase flows with complex interfaces and high density ratios", Computers & Mathematics with Applications, 2018 Publication	<1%
30	etheses.whiterose.ac.uk Internet Source	<1%
	kar.kent.ac.uk	

31	Internet Source	<1%
32	aip.scitation.org Internet Source	<1%
33	link.springer.com Internet Source	<1%
34	upcommons.upc.edu Internet Source	<1%
35	pure.tue.nl Internet Source	<1%
36	Liu, M B, and G R Liu. "Smoothed Particle Hydrodynamics — Methodology", Particle Methods for Multi-Scale and Multi-Physics, 2016. Publication	<1%
37	Submitted to University of Strathclyde Student Paper	<1%
38	freidok.uni-freiburg.de Internet Source	<1%
39	qdoc.tips Internet Source	<1%
40	tel.archives-ouvertes.fr Internet Source	<1%
41	Md. Aftabur Rahman, Kazuo Konagai. "A hands-on approach to estimate debris flow	<1%

velocity for rational mitigation of debris hazard", Canadian Geotechnical Journal, 2018
Publication

42	lemta.univ-lorraine.fr Internet Source	<1 %
43	Submitted to The Robert Gordon University Student Paper	<1 %
44	iccfd9.itu.edu.tr Internet Source	<1 %
45	nbn-resolving.de Internet Source	<1 %
46	"High Performance Computing in Science and Engineering ´16", Springer Science and Business Media LLC, 2016 Publication	<1 %
47	Submitted to Imperial College of Science, Technology and Medicine Student Paper	<1 %
48	digitalassets.lib.berkeley.edu Internet Source	<1 %
49	escholarship.org Internet Source	<1 %
50	sci-en-tech.com Internet Source	<1 %

51	Tiwari, S.. "Modeling of two-phase flows with surface tension by finite pointset method (FPM)", Journal of Computational and Applied Mathematics, 20070615 Publication	<1 %
52	link.aps.org Internet Source	<1 %
53	www.ift.org Internet Source	<1 %
54	Christoph Gissler, Andreas Henne, Stefan Band, Andreas Peer, Matthias Teschner. "An implicit compressible SPH solver for snow simulation", ACM Transactions on Graphics, 2020 Publication	<1 %
55	E. Plaza, Leonardo Di G. Sigalotti, Luis Pérez, Jorge Troconis, Wilfredo Angulo, María Castro. "Efficiency of particle search methods in smoothed particle hydrodynamics: a comparative study (part I)", Progress in Computational Fluid Dynamics, An International Journal, 2021 Publication	<1 %
56	Submitted to Kingston University Student Paper	<1 %
57	N. Grenier, D. Le Touzé, A. Colagrossi, M. Antuono, G. Colicchio. "Viscous bubbly flows	<1 %

simulation with an interface SPH model", Ocean Engineering, 2013
Publication

58	Submitted to Nelson Mandela Metropolitan University Student Paper	<1 %
59	Prapanch Nair, Gaurav Tomar. "Simulations of gas-liquid compressible-incompressible systems using SPH", Computers & Fluids, 2018 Publication	<1 %
60	Szewc, K., J. Pozorski, and J.-P. Minier. "Analysis of the incompressibility constraint in the smoothed particle hydrodynamics method : ANALYSIS OF THE INCOMPRESSIBILITY CONSTRAINT IN THE SPH METHOD", International Journal for Numerical Methods in Engineering, 2012. Publication	<1 %
61	doc.utwente.nl Internet Source	<1 %
62	Prapanch Nair, Thorsten Pöschel. "Dynamic capillary phenomena using Incompressible SPH", Chemical Engineering Science, 2018 Publication	<1 %
63	Submitted to University of Durham Student Paper	<1 %

64	Submitted to University of Leeds Student Paper	<1 %
65	Abdelraheem M. Aly, Mitsuteru Asai, Yoshimi Sonda. "Modelling of surface tension force for free surface flows in ISPH method", International Journal of Numerical Methods for Heat & Fluid Flow, 2013 Publication	<1 %
66	Submitted to Indian Institute of Science, Bangalore Student Paper	<1 %
67	Tartakovsky, A.M.. "Pore scale modeling of immiscible and miscible fluid flows using smoothed particle hydrodynamics", Advances in Water Resources, 200610 Publication	<1 %
68	eprints.nottingham.ac.uk Internet Source	<1 %
69	export.arxiv.org Internet Source	<1 %
70	iahr.tandfonline.com.tandf-prod.literatumonline.com Internet Source	<1 %
71	research.sabanciuniv.edu Internet Source	<1 %
72	wrap.warwick.ac.uk	

Internet Source

<1%

73	Ted Belytschko, Yong Guo, Wing Kam Liu, Shao Ping Xiao. "A unified stability analysis of meshless particle methods", International Journal for Numerical Methods in Engineering, 2000 Publication	<1%
74	fotonastenu.ru Internet Source	<1%
75	ftp.lstc.com Internet Source	<1%
76	hci.iwr.uni-heidelberg.de Internet Source	<1%
77	Abhinav Muta, Prabhu Ramachandran, Pawan Negi. "An efficient, open source, iterative ISPH scheme", Computer Physics Communications, 2020 Publication	<1%
78	Hu, X.Y.. "A multi-phase SPH method for macroscopic and mesoscopic flows", Journal of Computational Physics, 20060410 Publication	<1%
79	Lijing Yang, Milad Rakhsha, Dan Negrut. "Comparison of Surface Tension Models in Smoothed Particles Hydrodynamics Method",	<1%

Volume 6: 15th International Conference on Multibody Systems, Nonlinear Dynamics, and Control, 2019
Publication

80	S.C. Wang, C.K. Chan, S.P. Li. "A vectorized algorithm on the ETA-10Q for MD simulation of particles in a box interacting by long-ranged forces", Computer Physics Communications, 1990 Publication	<1 %
81	www.flow3d.com Internet Source	<1 %
82	Libin Liang, Pu Zhang, Hui Ding, Guangzhi Wang. "An improved method of calculating MTF from PSF based on CT phantom images", 2nd IET International Conference on Biomedical Image and Signal Processing (ICBISP 2017), 2017 Publication	<1 %
83	Meng Shuangshuang, Hassan Frissane, Lorenzo Taddei, Nadhir Lebaal, Sebastien Roth. "The study on performances of kernel types in solid dynamic problems by smoothed particle hydrodynamics", Computational Particle Mechanics, 2020 Publication	<1 %
84	Submitted to University of Exeter Student Paper	<1 %

85	Xiaoyang Xu. "An improved SPH approach for simulating 3D dam-break flows with breaking waves", Computer Methods in Applied Mechanics and Engineering, 2016 Publication	<1 %
86	Yixin Lin, G.R. Liu, Guangyu Wang. "A particle-based free surface detection method and its application to the surface tension effects simulation in smoothed particle hydrodynamics (SPH)", Journal of Computational Physics, 2019 Publication	<1 %
87	Hu, X.Y.. "An incompressible multi-phase SPH method", Journal of Computational Physics, 20071110 Publication	<1 %
88	Satori Tsuzuki. " Particle approximation of the two-fluid model for superfluid He using smoothed particle hydrodynamics ", Journal of Physics Communications, 2021 Publication	<1 %
89	So-Hyun Park, Young Beom Jo, Yelyn Ahn, Hae Yoon Choi, Tae Soo Choi, Su-San Park, Hee Sang Yoo, Jin Woo Kim, Eung Soo Kim. "Development of Multi-GPU–Based Smoothed Particle Hydrodynamics Code for Nuclear Thermal Hydraulics and Safety: Potential and	<1 %

Challenges", Frontiers in Energy Research, 2020
Publication

90	Stephen B. Foulkes. "SPH simulations of irradiation-driven warped accretion discs and the long periods in X-ray binaries", Monthly Notices of the Royal Astronomical Society, 01/11/2010 Publication	<1 %
91	Submitted to UNESCO-IHE Institute for Water Education Student Paper	<1 %
92	hal.univ-lorraine.fr Internet Source	<1 %
93	Abdelkader Krimi, Mehdi Rezoug, Sofiane Khelladi, Xesús Nogueira, Michael Deligant, Luis Ramírez. "Smoothed Particle Hydrodynamics: A consistent model for interfacial multiphase fluid flow simulations", Journal of Computational Physics, 2018 Publication	<1 %
94	Submitted to University of Melbourne Student Paper	<1 %
95	Walter Dehnen, Hossam Aly. "Improving convergence in smoothed particle hydrodynamics simulations without pairing	<1 %

instability", Monthly Notices of the Royal Astronomical Society, 2012
Publication

---

96 www.ama-science.org <1%
Internet Source

---

97 Dong, Tianwen, and Shunliang Jiang. "Comparisions of Mirror and Static Boundary Conditions in Incompressible Smoothed Particle Hydrodynamics", 2010 International Conference on Computational and Information Sciences, 2010. <1%
Publication

---

98 J. J. Elmendorp, R. J. Maalcke. "A study on polymer blending microrheology: Part 1", Polymer Engineering and Science, 1985 <1%
Publication

---

99 M. B. LIU, G. R. LIU, Z. ZONG. "AN OVERVIEW ON SMOOTHED PARTICLE HYDRODYNAMICS", International Journal of Computational Methods, 2011 <1%
Publication

---

100 Santosh Konangi, Nikhil K. Palakurthi, Nikolaos K. Karadimitriou, Ken Comer, Urmila Ghia. "Comparison of pore-scale capillary pressure to macroscale capillary pressure using direct numerical simulations of drainage under dynamic and quasi-static conditions", Advances in Water Resources, 2021 <1%

Publication

101	"Aerosols - Science and Technology", Wiley, 2010 Publication	<1 %
102	Erin Arai, Alexandre Tartakovsky, R. Glynn Holt, Sheryl Grace, Emily Ryan. "Comparison of Surface Tension Generation Methods in Smoothed Particle Hydrodynamics for Dynamic Systems", Computers & Fluids, 2020 Publication	<1 %
103	Yasutomo Kanetsuki, John C. Wells, Susumu Nakata. "Efficient local smoothed particle hydrodynamics with precomputed patches", International Journal of Computer Mathematics, 2018 Publication	<1 %
104	Zhang, M.. "Simulation of surface tension in 2D and 3D with smoothed particle hydrodynamics method", Journal of Computational Physics, 20100920 Publication	<1 %
105	media.proquest.com Internet Source	<1 %
106	publikationen.uni-tuebingen.de Internet Source	<1 %
107	zh.scribd.com Internet Source	<1 %

108	Abdelraheem M. Aly, Mitsuteru Asai. "Modelling of Non-Darcy Flows through Porous Media Using Extended Incompressible Smoothed Particle Hydrodynamics", Numerical Heat Transfer, Part B: Fundamentals, 2014 Publication	<1 %
109	B.X. Zheng, Z. Chen. "A Multiphase smoothed particle hydrodynamics model with lower numerical diffusion", Journal of Computational Physics, 2019 Publication	<1 %
110	Fedir V. Sirotkin, Jack J. Yoh. "A new particle method for simulating breakup of liquid jets", Journal of Computational Physics, 2012 Publication	<1 %
111	L.P. Yarin, A. Mosyak, G. Hetsroni. "Chapter 6 Boiling in Micro-Channels", Springer Science and Business Media LLC, 2009 Publication	<1 %
112	Rafiee, Ashkan, Sharen Cummins, Murray Rudman, and Krish Thiagarajan. "The Effect of Pressure Solution in SPH Simulations of Sloshing Flow", Volume 6 Ocean Engineering, 2011. Publication	<1 %
113	Rui Xu, Peter Stansby, Dominique Laurence. "Accuracy and stability in incompressible SPH	<1 %

(ISPH) based on the projection method and a new approach", Journal of Computational Physics, 2009
Publication

114	pdfs.semanticscholar.org Internet Source	<1%
115	www.dip.fau.de Internet Source	<1%
116	www.hamburg.baw.de Internet Source	<1%
117	A. TSUCHIYA. "Performance Limitation of On-Chip Global Interconnects for High-Speed Signaling", IEICE Transactions on Fundamentals of Electronics Communications and Computer Sciences, 04/01/2005 Publication	<1%
118	A. Zainali, N. Tofighi, M.S. Shadloo, M. Yildiz. "Numerical investigation of Newtonian and non-Newtonian multiphase flows using ISPH method", Computer Methods in Applied Mechanics and Engineering, 2013 Publication	<1%
119	Ahmed A. Shabana. "Computational Dynamics", Wiley, 2010 Publication	<1%
120	Chong Peng, Christoph Bauinger, Kamil Szewc, Wei Wu, Hui Cao. "An improved	<1%

predictive-corrective incompressible smoothed particle hydrodynamics method for fluid flow modelling", Journal of Hydrodynamics, 2019
Publication

---

121 Environmental Science and Engineering, 2014. <1%
Publication

---

122 Lobovsky, L.. "Smoothed particle hydrodynamics and finite volume modelling of incompressible fluid flow", Mathematics and Computers in Simulation, 20071012 <1%
Publication

---

123 M.L. Hosain, J.M. Domínguez, R. Bel Fdhila, K. Kyprianidis. "Smoothed particle hydrodynamics modeling of industrial processes involving heat transfer", Applied Energy, 2019 <1%
Publication

---

124 Qianhong Yang, Jun Yao, Zhaoqin Huang, Mehmood Asif. "A comprehensive SPH model for three-dimensional multiphase interface simulation", Computers & Fluids, 2019 <1%
Publication

---

125 Wen-Bin Liu, Dong-Jun Ma, Ming-Yu Zhang, An-Min He, Nan-Sheng Liu, Pei Wang. "A new surface tension formulation in smoothed particle hydrodynamics for free-surface flows", Journal of Computational Physics, 2021 <1%

	Publication	
126	academic.oup.com Internet Source	<1 %
127	cronfa.swan.ac.uk Internet Source	<1 %
128	dr.ntu.edu.sg Internet Source	<1 %
129	eprints.whiterose.ac.uk Internet Source	<1 %
130	infoscience.epfl.ch Internet Source	<1 %
131	iopscience.iop.org Internet Source	<1 %
132	journals.vgtu.lt Internet Source	<1 %
133	kluedo.ub.uni-kl.de Internet Source	<1 %
134	repository.tudelft.nl Internet Source	<1 %
135	scholars.unh.edu Internet Source	<1 %
136	www.actapress.com Internet Source	<1 %
137	www.icvt.uni-stuttgart.de	

Internet Source

<1%

138 A. Gastelum, M. Krueger, J. Marquez, G. Gimel'farb, P. Delmas. "Automatic 3D lip shape segmentation and modelling", 2008 23rd International Conference Image and Vision Computing New Zealand, 2008

Publication

<1%

139 Christoph Meier, Sebastian L. Fuchs, A. John Hart, Wolfgang A. Wall. "A novel smoothed particle hydrodynamics formulation for thermo-capillary phase change problems with focus on metal additive manufacturing melt pool modeling", Computer Methods in Applied Mechanics and Engineering, 2021

Publication

<1%

140 D. E. Keller, A. M. Fischer, C. Frei, M. A. Liniger, C. Appenzeller, R. Knutti. "Stochastic modelling of spatially and temporally consistent daily precipitation time-series over complex topography", Copernicus GmbH, 2014

Publication

<1%

141 Jinlian Ren, Jie Ouyang, Tao Jiang, Qiang Li. "A corrected symmetric SPH method to simulate viscoelastic free surface flows based on the PTT model", International Journal for Numerical Methods in Fluids, 2012

Publication

142 Julia Mang, Helmut Küchenhoff, Sabine Meinck, Manfred Prenzel. "Sampling weights in multilevel modelling: an investigation using PISA sampling structures", Large-scale Assessments in Education, 2021 <1 %
Publication

143 Liu, M B, and G R Liu. "Smoothed Particle Hydrodynamics — Applications", Particle Methods for Multi-Scale and Multi-Physics, 2016. <1 %
Publication

144 Shuai Chen, Wei Niu. "On different calculation formulas of the pressure term in bi-phase SPH simulations", AIP Advances, 2018 <1 %
Publication

145 Sun, Pengnan, Furen Ming, and Aman Zhang. "Numerical simulation of interactions between free surface and rigid body using a robust SPH method", Ocean Engineering, 2015. <1 %
Publication

146 Szewc, K., J. Pozorski, and J.-P. Minier. "Spurious interface fragmentation in multiphase SPH : SPURIOUS INTERFACE FRAGMENTATION IN MULTIPHASE SPH", International Journal for Numerical Methods in Engineering, 2015. <1 %

Publication

147	Tartakovsky, A.M.. "A smoothed particle hydrodynamics model for miscible flow in three-dimensional fractures and the two-dimensional Rayleigh-Taylor instability", Journal of Computational Physics, 20050810 Publication	<1 %
148	Tibing Xu, Yee-Chung Jin. "Improvement of a projection-based particle method in free-surface flows by improved Laplacian model and stabilization techniques", Computers & Fluids, 2019 Publication	<1 %
149	Tsuyoshi Hattori, Masaharu Sakai, Shigeru Akaike, Seiichi Koshizuka. "Numerical simulation of droplet sliding on an inclined surface using moving particle semi-implicit method", Computational Particle Mechanics, 2018 Publication	<1 %
150	Submitted to University of Bristol Student Paper	<1 %
151	Submitted to University of Southampton Student Paper	<1 %
152	elib.uni-stuttgart.de Internet Source	<1 %

en.wikipedia.org

153	Internet Source	<1%
154	mts.intechopen.com Internet Source	<1%
155	nordicrheologysociety.org Internet Source	<1%
156	thesis.library.caltech.edu Internet Source	<1%
157	www.diss.fu-berlin.de Internet Source	<1%
158	www.escholar.manchester.ac.uk Internet Source	<1%
159	www.ideals.illinois.edu Internet Source	<1%
160	www.osti.gov Internet Source	<1%
161	Geo-disaster Modeling and Analysis An SPH-based Approach, 2014. Publication	<1%
162	Jannes Kordilla, Torsten Noffz, Marco Dentz, Tobias Geyer, Alexandre M. Tartakovsky. "Effect of Unsaturated Flow Modes on Partitioning Dynamics of Gravity-Driven Flow at a Simple Fracture Intersection: Laboratory Study and Three-Dimensional Smoothed	<1%

Particle Hydrodynamics Simulations", Water Resources Research, 2017
Publication

163 M. X. Rodriguez-Paz. "A corrected smooth particle hydrodynamics method for the simulation of debris flows", Numerical Methods for Partial Differential Equations, 01/2004 <1 %
Publication

164 Shadloo, M.S.. "Improved Incompressible Smoothed Particle Hydrodynamics method for simulating flow around bluff bodies", Computer Methods in Applied Mechanics and Engineering, 20110201 <1 %
Publication

165 Wen Zheng, Bo Zhu, Byungmoon Kim, Ronald Fedkiw. "A new incompressibility discretization for a hybrid particle MAC grid representation with surface tension", Journal of Computational Physics, 2015 <1 %
Publication

166 Zhang, Aman, Pengnan Sun, and Furen Ming. "An SPH modeling of bubble rising and coalescing in three dimensions", Computer Methods in Applied Mechanics and Engineering, 2015. <1 %
Publication

167	Daiane Iglesia Dolci. "Análises de sensibilidade e estabilidade baseadas no método adjunto aplicadas para problemas de fluidodinâmica e problemas de interação fluido-estrutura.", Universidade de Sao Paulo, Agencia USP de Gestao da Informacao Academica (AGUIA), 2020 Publication	<1 %
168	Gureghian, A.B.. "Simultaneous transport of water and reacting solutes through multilayered soils under transient unsaturated flow conditions", Journal of Hydrology, 197905 Publication	<1 %
169	Mingyu Zhang, Xiao-Long Deng, Zhijun Shen. "A robust sharp interface method for SPH", Engineering Analysis with Boundary Elements, 2019 Publication	<1 %
170	Paul Meakin. "Particle methods for simulation of subsurface multiphase fluid flow and biogeochemical processes", Journal of Physics Conference Series, 07/01/2007 Publication	<1 %
171	Seungho Baek, JungHyun Han. "Simulation of thin liquid jets with threads", Computer Animation and Virtual Worlds, 2017 Publication	<1 %

172	Zeinab El-Sayegh, Moustafa El-Gindy, Inge Johansson, Fredrik Öijer. "Modelling tire-moist terrain interaction using advanced computational techniques", Journal of Terramechanics, 2020 Publication	<1 %
173	mediatum.ub.tum.de Internet Source	<1 %

Exclude quotes	Off	Exclude matches	Off
Exclude bibliography	Off		